A SEARCH FOR A LEPTON-NUMBER-VIOLATING DECAY OF THE CASCADE-MINUS HYPERON

BY

DURGAPRASAD RAJARAM

Submitted in partial fulfillment of the
requirements for the degree of
Doctor of Philosophy in Physics
in the Graduate College of the
Illinois Institute of Technology

Approved _____
Adviser

ORIGINAL ARCHIVAL COPY

Chicago, Illinois
May, 2002

ILLINOIS INSTITUTE OF TECHNOLOGY
PAUL V. GALVIN LIBRARY
IIT CENTER
CHICAGO, IL 60616

TABLE OF CONTENTS

Page

ACKNOWLEDGMENT iii

LIST OF FIGURES vi

LIST OF TABLES ix

CHAPTER

I. INTRODUCTION 1

The Standard Model 1
Lepton-Number Conservation 3
Current Knowledge And Possible Searches 6

II. THE HYPERCP EXPERIMENT 9

The Tevatron At Fermilab 9
Beam Description, Monitoring, Profile 9
Target 10
Collimator 10
Decay Pipe 12
Wire Chambers 12
Analysis Magnets 14
Hodoscopes 14
Calorimeter 15
Muon System 15
Trigger 16
Data Acquisition System 16
Summary Of Data Collected 18

III. DATA PROCESSING AND SELECTION 19

Track Finding 19
Data Reduction 20
Muon Selection 21
Muon Detector Efficiencies 24
DST Production 25
Final Selection Cuts 26

IV. ANALYSIS II 42

Monte Carlo 42
Comparison Of MC With Data 53
Normalization 54

CHAPTER Page

Backgrounds 63
Triggers 63
Systematics 64
Calculating The Branching Ratio 74

V. CONCLUSION 78

REFERENCES 80

LIST OF FIGURES

Figure		Page
1.1.	A possible diagram for the decay $\Xi^- \to p\mu^-\mu^-$	7
2.1.	The HyperCP hyperon channel	11
2.2.	Elevation and Plan Views of the HyperCP Spectrometer	13
3.1.	Absolute Difference between Projected Track Position and Proportional Tube Hits in the Front Muon Chamber	22
3.2.	Absolute Difference between Projected Track Position and Hodoscope Hits At the Muon Hodoscope	23
3.3.	Invariant $p\mu^-\mu^-$ Mass Distribution for Three-track Events in Stream-7 Before Applying Any Cuts	27
3.4.	Distribution of Total Ξ^- momentum	29
3.5.	Momentum of the OS Track as a Fraction of the Total Momentum for $\Xi^- \to \Lambda\pi^-$ and $K^- \to \pi^-\pi^-\pi^+$ Decays	30
3.6.	Distribution of the Reconstructed $\Lambda\pi^-$ Invariant Mass	32
3.7.	Distribution of the Reconstructed $\pi^-\pi^-\pi^+$ Invariant Mass	33
3.8.	Distribution of the z Position of the Decay Vertex for $\Xi^{-}\to\Lambda\pi^-$ Decays	34
3.9.	Average Distance between Tracks at the z of the Decay Vertex for $\Xi^- \to \Lambda\pi^-$ and $K^- \to \pi^-\pi^-\pi^+$ Decays	35
3.10.	$\chi^2/ndof$ from Single-vertex Fit for $\Xi^- \to \Lambda\pi^-$ and $K^- \to \pi^-\pi^-\pi^+$ Decays. The Arrow Indicates the Location of the Cut	36
3.11.	Projected x Position of Ξ^- at the Target	38
3.12.	Projected y Position of the Ξ^- at the Target	40
4.1.	Invariant $p\mu^-\mu^-$ Mass Distribution from a Monte Carlo Simulation of the Decay	44
4.2.	Invariant $p\mu^-\mu^-$ Mass Distribution and a Fit to the Distribution from Monte Carlo Simulation	45

Figure Page

4.3. Monte Carlo Generated $p\mu^-\mu^-$ decays Reconstructed as $p\pi^-\pi^-$ Events 46

4.4. Monte Carlo Generated $p\mu^-\mu^-$ Decays Reconstructed as $\pi^+\pi^-\pi^-$ Events 47

4.5. MC Distribution of p_{total} for $\Xi^- \rightarrow p\mu^-\mu^-$ Events 48

4.6. MC distribution of the x Position of Ξ^- at the Target for $\Xi^- \rightarrow p\mu^-\mu^-$ Events 49

4.7. MC distribution of the y Position of Ξ^- at the Target for $\Xi^- \rightarrow p\mu^-\mu^-$ Events 50

4.8. MC distribution of the z of the Ξ^- Decay Vertex for $\Xi^- \rightarrow p\mu^-\mu^-$ Events 51

4.9. MC distribution of the Average Distance between Tracks at the Common Vertex for $\Xi^- \rightarrow p\mu^-\mu^-$ Events 52

4.10. MC and Data Distributions of p_{total} for $\Xi^- \rightarrow \Lambda\pi^-$ Events after matching for Run #2200 54

4.11. MC and Data distributions of p_x for $\Xi^- \rightarrow \Lambda\pi^-$ Events 55

4.12. MC and data Distributions of p_y for $\Xi^- \rightarrow \Lambda\pi^-$ Events 56

4.13. MC and Data Distributions of the x Position of the Ξ^- Hyperon at Target, for $\Xi^- \rightarrow \Lambda\pi^-$ Events 57

4.14. MC and Data Distributions of the y Position of the Ξ^- Hyperon at Target, for $\Xi^- \rightarrow \Lambda\pi^-$ Events 58

4.15. MC and Data Distributions of the z Position of the Ξ^- Decay Vertex, for $\Xi^- \rightarrow \Lambda\pi^-$ Events 59

4.16. MC and Data Distributions of the First Pion at the Location of the Second Muon Steel Block 60

4.17. MC and Data Distributions of the Second Pion at the Location of the Second Muon Steel Block 61

4.18. Invariant $p\pi^-\pi^-$ Mass Distribution. This is the Normalization Data-set 65

Figure Page

4.19. x Distribution of the the Proton from $\Xi^- \rightarrow \Lambda\pi^-$, $\Lambda \rightarrow p\pi^-$ at the Front Face of the Calorimeter 66

4.20. x Distribution of the Proton from $\Xi^- \rightarrow p\mu^-\mu^-$ at the Front Face of the Calorimeter 67

4.21. Variation in Relative Acceptance between $\Xi^- \rightarrow p\mu^-\mu^-$ and $\Xi^- \rightarrow \Lambda\pi^-$ Modes Due to Variation in Beam Targeting in x 68

4.22. Variation in Relative Acceptance between $\Xi^- \rightarrow p\mu^-\mu^-$ and $\Xi^- \rightarrow \Lambda\pi^-$ Modes Due to Variation in Beam Targeting in y 69

4.23. Distribution of Upstream Muon Proportional Tube Efficiencies as a Function of Run Number 70

4.24. Distribution of Midstream Muon Proportional Tube Efficiencies as a Function of Run Number 71

4.25. Distribution of Downstream Muon Proportional Tube Efficiencies as a Function of Run Number 72

4.26. Distribution of Muon Hodoscope Efficiencies as a Function of Run Number 73

4.27. $p\mu^-\mu^-$ Invariant Mass Distribution After Applying All Selection Cuts 77

LIST OF TABLES

Table		Page
3.1.	Output Streams	20
3.2.	Summary of Selection Cuts	41
3.3.	Cut Efficiencies	41
4.1.	Efficiencies of Selection Cuts	53
4.2.	Relative Efficiencies for the Detection of $\Xi^- \to \Lambda\pi^-$ and $\Xi^- \to p\mu^-\mu^-$ Decay Modes	75
4.3.	Summary of Systematic Uncertainties	76

CHAPTER I

INTRODUCTION

The conservation of lepton numbers, along with the related issues of lepton flavor mixing and neutrino masses, remains one of the fundamental puzzles in physics [1, 2, 3]*. While experimental data has indicated that lepton number should be conserved, the reason is not fully understood. In the following sections the ideas of lepton number conservation, the related issue of neutrino mass, the status of searches for lepton number violation, and the motivation for the present analysis will be discussed.

1.1 The Standard Model

The Standard Model describes the strong, weak, and electromagnetic interactions of quarks and leptons, the fundamental constituents of nature. The interactions are mediated by particles of integral spin known as gauge bosons. The model is based on the gauge group $SU(3)_C \times SU(2)_L \times U(1)_Y$. Quantum chromodynamics, the theory of strong interactions based on the $SU(3)$ gauge group, describes the quark sector of the model, while the $SU(2)_L \times U(1)_Y$ group is the basis for the unified theory of electromagnetic and weak interactions [4, 5, 6]. Quarks are spin-$\frac{1}{2}$ particles that carry fractional charges $\frac{2}{3}e$ or $-\frac{1}{3}e$ and come in six different varieties, called flavors: up (u), down (d), strange (s), charmed (c), bottom (or beauty), (b), and top (or truth), (t). Further, each quark flavor comes in three colors. The strong force between quarks is also referred to as the color force. The six quarks are grouped in three doublets referred to as generations:

$$\begin{pmatrix} u \\ d \end{pmatrix} \begin{pmatrix} c \\ s \end{pmatrix} \begin{pmatrix} t \\ b \end{pmatrix}$$

*Corresponding to references in the bibliography

Each quark also carries another quantum number known as baryon number (B). All quarks have $B = 1/3$. The interactions involving quarks and the mediating bosons (gluons) is based on the gauge group $SU(3)_C$, where the subscript C refers to the color force between quarks and gluons. Quarks don't appear in a free state but rather appear in nature only as constituents of composite particles (hadrons). Quarks can combine in two different ways: $q\bar{q}$ combinations (mesons), and qqq combinations (baryons). Baryons composed of one or more strange quarks are known as hyperons. Thus, for example, a pion ($\pi^+ = u\bar{d}$) is a meson composed of the up and anti-down quarks, while the cascade ($\Xi^- = dss$) is a hyperon. Hadrons, apart from experiencing the strong force, can also participate in electromagnetic and weak interactions.

Leptons, like quarks, are spin-$\frac{1}{2}$ particles that are either neutral or carry integral charges of $\pm e$. Analogous to the three generations of quarks, there are six kinds of leptons: electrons (e), muons (μ), taus (τ), and three neutrinos (ν), one associated with each of the above leptons. The leptons are also grouped in three generations:

$$\begin{pmatrix} \nu_e \\ e \end{pmatrix} \begin{pmatrix} \nu_\mu \\ \mu \end{pmatrix} \begin{pmatrix} \nu_\tau \\ \tau \end{pmatrix}$$

The e, μ, and τ carry charges of $-e$, while the neutrinos are neutral. Every lepton is assigned a quantum number called lepton number (L_e, L_μ, L_τ). $L_{e,\mu,\tau} = 1$. There is also a total lepton number (L) which is just the sum of the lepton numbers of the particles involved in an interaction.

The mediators of the weak force are the charged and neutral gauge bosons $W^\pm$ and Z^0, and electromagnetic interactions are mediated by neutral photons. In addition to quarks, leptons, and gauge bosons, there is one other particle which completes the description of the strong and electroweak forces. This is the scalar (spin-0) boson, known as the Higgs particle, which arises as a result of the spontaneous breakdown of the $SU(2)_L \times U(1)_Y$ symmetry via the Higgs mechanism. The Higgs has not been observed and the search for its existence is continuing.

1.2 Lepton-Number Conservation

In the Standard Model, individual lepton family numbers and total lepton number are conserved. While this is consistent with what has been observed in physical phenomena, it is not clearly understood why lepton number should be conserved. Also, lepton number conservation, unlike global conservation laws like that for electric charge, is not associated with any local gauge invariance. As a result, the theoretical basis for the conservation of lepton number is weak.

This is in contrast with the quark sector where individual flavors of hadrons are not conserved in weak interactions. In the $SU(2)_L \times U(1)_Y$ electroweak theory, quarks and leptons are placed in left-handed doublets and right-handed singlets.

$$\begin{pmatrix} u \\ d' \end{pmatrix}_L, \begin{pmatrix} c \\ s' \end{pmatrix}_L, \begin{pmatrix} t \\ b' \end{pmatrix}_L \begin{pmatrix} \nu_e \\ e \end{pmatrix}_L, \begin{pmatrix} \nu_\mu \\ \mu \end{pmatrix}_L, \begin{pmatrix} \nu_\tau \\ \tau \end{pmatrix}_L, (e, \mu, \tau)_R.$$

However, the weak interaction eigenstates of the quarks (states denoted with primes in the above doublet representation) are not identical with the strong interaction mass eigenstates due to the spontaneous breakdown of the $SU(2)_L \times U(1)_Y$ symmetry. The relation between the two states is described in terms of a mixing matrix known as the Cabbibo-Kobayashi-Maskawa (CKM) matrix [7, 8]. Conventionally, the 3×3 unitary matrix is represented as:

$$\begin{pmatrix} d' \\ s' \\ b' \end{pmatrix} = \begin{vmatrix} V_{ud} & V_{us} & V_{ub} \\ V_{cd} & V_{cs} & V_{cb} \\ V_{td} & V_{ts} & V_{tb} \end{vmatrix} \begin{pmatrix} d \\ s \\ b \end{pmatrix}$$

where the mass eigenstates are the unprimed ones. In the CKM parameterization of the matrix, there are three real angles and one complex phase which can be determined experimentally. As a result of the mixing, hadron flavors are not conserved in weak interactions involving quarks.

As mentioned earlier, individual flavors are not conserved in interactions involving leptons. Neutrinos seem to appear in nature in states of definite helicity: the neutrino is always left-handed (spin is along the direction of momentum in the sense of a left-handed screw) and the anti-neutrino is right-handed (spin is in the direction of momentum in a right-handed system). Thus, in the Standard Model description of electroweak interactions, neutrinos appear only as components of left-handed doublets and are taken to be exactly massless. If neutrinos had mass (*i.e.* if they don't travel at the speed of light), then it would be possible to Lorentz-transform to a different reference frame and flip the helicity. According to the superposition postulate of quantum mechanics the interaction states ($\nu_j, j = e, \mu, \tau$) would be combinations of mass eigenstates (ν_1, ν_2, ν_3):

$$\nu_j = \sum_{i=1}^{3} V_{ji}\nu_i$$

where the unitary matrix V_{ji} describes the mixing between neutrino flavors, similar to the CKM matrix for quarks. If neutrinos oscillate, individual lepton family numbers, and hence the total lepton number, would no longer have to be conserved quantum numbers.

To futher understand the issue of neutrino mass and its relation to lepton number violation, it is helpful to consider the $SU(2)_L \times U(1)_Y$ formulation in more detail and see how particles acquire masses in the Standard Model. Dirac mass terms can be thought of as transitions between left-handed and right-handed states. Initially, all particles start off massless in vacuum. The $SU(2)_L \times U(1)_Y$ symmetry of the vacuum is then spontaneously broken via the Higgs mechanism which is introduced by incorporating a doublet of scalar Higgs fields $\Phi = \begin{pmatrix} \phi^+ \\ \phi^\circ \end{pmatrix}$. As a result, the Higgs field acquires a vacuum expectation value $< \Phi >_0 = \begin{pmatrix} 0 \\ \frac{v}{\sqrt{2}} \end{pmatrix}$, where $v =< \phi^\circ >$ is the vacuum expectation value of the neutral component of the Higgs doublet and is a measure of the weak scale ($v = 246$ GeV/c^2). The new Higgs field after the breakdown of symmetry can be written as $\Phi = \begin{pmatrix} 0 \\ \frac{\chi+v}{\sqrt{2}} \end{pmatrix}$, where χ is the physical

Higgs scalar field that remains after the spontaneous breakdown of symmetry. The interaction terms of the Lagrangian can be written as:

$$\mathcal{L} = \frac{1}{2}h_w(\overline{\psi_L})\Phi\psi_R + h.c. \tag{1-1}$$

$$= \frac{1}{2}h_w\overline{\psi_L}m\psi_R + \frac{1}{2\sqrt{2}}h_w\overline{\psi_L}\chi\psi_R + h.c. \tag{1-2}$$

where h_w is the Yukawa coupling of the particle to the scalar Higgs field. The interaction with the neutral component of the Higgs field results in the particle acquiring a Dirac mass $m = h_w v/\sqrt{2}$. In the case of the neutrino, since it appears only in the left-handed doublet it is not possible to form a Dirac mass term of the form $m\bar{\nu}_L\nu_R$ in the existing model.

Experimental evidence from the Super-Kamiokande and LSND [9, 10, 11] experiments, and most recently from the Sudbury Neutrino Observatory (SNO) [12] seem to indicate that neutrinos do indeed oscillate. The Super-Kamiokande experiment and SNO measure the atmospheric neutrino flux, while LSND searches for $\nu_\mu \to \nu_e$ oscillation in an accelarator beam. Super-K and SNO are also sensitive to probing for evidence of sterile neutrinos by studying the oscillation of ν_μ to ν_τ. The evidence for neutrino oscillation is exciting news since it opens the door to new physics beyond the Standard Model and helps understand neutrino masses and mixing.

There are several ways in which the Standard Model can be extended to allow for lepton number violation and the generation of neutrino masses [2, 13, 14, 15]. Most models allow for a mass term associated with a massive neutrino [16], first postulated by Majorana, which is its own anti-particle and is associated with a Majorana field which is a *CP* eigenstate. Thus, a Majorana neutrino has two states (spin-up and spin-down) and transforms identically under Lorentz and *CP* transformations. Dirac neutrinos, on the other hand, would have four states (spin-up and spin-down for the particle and anti-particle) and transform differently under Lorentz and *CP* transformations. Thus, a transition between the two states of a Majorana neutrino involves a change in L by 2 units. In fact, $\Delta L = 2$ implies the existence of Majorana

neutrinos of non-zero mass [17, 14]. Understanding the conservation of total lepton number and searching for experimental evidence of the violation of lepton number are therefore both interesting and of fundamental importance, especially so in light of new results from neutrino oscillation experiments.

1.3 Current Knowledge And Possible Searches

Neutrinoless double-beta decays provide the best upper limits on lepton number conservation in cases where the lepton involved is an electron. A double beta decay is a nuclear transition of the form

$$(Z, A) \rightarrow (Z + 2, A) + 2e^- + 2\overline{\nu}_e$$

where the nuclear transition is accompanied by the emission of two electrons and two anti-neutrinos. While this kind of decay conserves lepton number, there is another way by which double beta decays can proceed. That is the neutrinoless double beta decay ($0\nu\beta\beta$)

$$(Z, A) \rightarrow (Z + 2, A) + 2e^-$$

which violates L by 2 units and is forbidden in the standard formulation of electroweak interactions. Regardless of how such a decay is mediated, the observation of lepton number violation by 2 units implies a Majorana neutrino [17] and points to physics beyond the Standard Model [18]. What is measured in $0\nu\beta\beta$ decay experiments is a half-life for the decay that is then used to set a limit on an effective Majorana mass ($<m_\nu>$) which is a function of neutrino-mixing parameters and neutrino mass eigenvalues. So far there has been no observation of $0\nu\beta\beta$ decays and the current best limit is $t_{1/2} > 1.8 \times 10^{25}$ yr (CL=90%) for the $0\nu\beta\beta$ decay of ^{76}Ge [19]. This corresponds to $<m_\nu>$ less than 0.36 eV.

Apart from $0\nu\beta\beta$ decay experiments, there are other particle decays which can be searched for as a test of lepton number conservation. While the double-beta decays are the most sensitive searches for lepton-number violation where the lepton is an electron, decays of the type $H_1 \rightarrow H_2\mu\mu$, where $H_{1,2}$ refer to hadrons, offer a different channel for exploring lepton number violation. Further, these decays are not constrained by the stringent limits set by $0\nu\beta\beta$ decays, nor are they limited by the rate of conversion of $\mu^- \rightarrow e^+$. The decay $\Xi^- \rightarrow p\mu^-\mu^-$ is one such decay and is the subject of the present analysis. Figure 1.1 shows one possible mechanism by which this decay can proceed. ν_M in the diagram refers to a Majorana neutrino

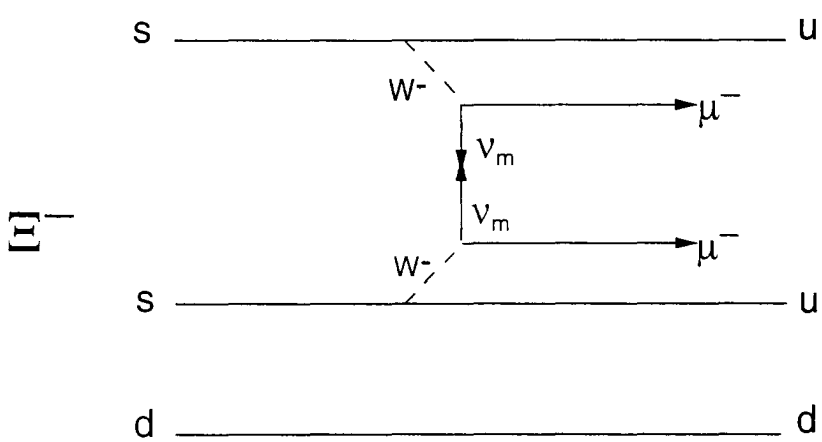

Figure 1.1 A possible diagram for the decay $\Xi^- \rightarrow p\mu^-\mu^-$

which mediates the $\Delta L = 2$ transition. As mentioned earlier [17], a change in lepton number by 2 units implies a massive neutrino of the Majorana type.

Whereas $0\nu\beta\beta$ decays have been, and are being, studied in considerable detail, very little experimental effort has gone into searches for other lepton-number-violating decays. Where the parent particle is a baryon, the lack of experimental knowledge is acute. To date, there has been no search for $\Delta L = 2$ processes in hyperon decays. The current limit ($< 4 \times 10^{-4}$) on the branching fraction for the decay comes from a retroactive analysis of data [21] from an experiment performed at Brookhaven National Laboratory (BNL) in 1974 [22]. HyperCP, the experiment whose data are

used in the present analysis has accumulated orders of magnitude more data than the BNL experiment and is an attractive place to perform a sensitive search for $\Delta L = 2$ hyperon decays. Any evidence of lepton number violation in the HyperCP experiment would open a wide range of exciting possibilities beyond the Standard Model.

CHAPTER II

THE HYPERCP EXPERIMENT

Experiment E-871 (HyperCP) was a fixed-target experiment performed at the Fermi National Accelerator Laboratory (FNAL) between 1997 and 1999 in two runs. The primary goal of the experiment is the search for direct *CP* violation in the decays of the charged hyperons Ξ^- ($\overline{\Xi}^+$). The data used in the current analysis were recorded by the experiment in its first run between April and August of 1997. We describe the experiment and the spectrometer in the following sections.

The laboratory coordinate system used to describe the spectrometer is a right-handed coordinate system with z pointing along the secondary beam and y perpendicular to z and pointing up.

2.1 The Tevatron At Fermilab

HyperCP was performed with a beam of protons accelerated to an energy of 800 GeV/c in the FNAL Tevatron and delivered to the experimental area. The HyperCP spectrometer was located in the Meson Center beam line. The deceleration and acceleration cycle lasted for 40 seconds and the extracted protons were made available to the experiment in "spills" of 20 s. The first few seconds of the spill were not used since they contained a series of high intensity "pings." The effective spill time in the experiment was, thus, approximately 19 s.

2.2 Beam Description, Monitoring, Profile

Typically, the intensity of protons incident on the target was 1.5×10^{11} s^{-1}. The intensity of the beam was monitored using ion chambers (IC). The spatial stability of the beam in the x and y directions was monitored with the help of two segmented wire ion chambers (SWICs) placed upstream of the target. The wire pitch of the SWIC was 0.5 mm and the first one was located approximately 20 cm from the target with the second SWIC 245.0 cm upstream of the first.

2.3 Target

A 2 mm × 2 mm copper target, either 2 cm or 6 cm long was used. The 2 cm-long target was used to produce Ξ^- hyperons while the longer target was used for the production of $\bar{\Xi}^+$ particles. The lengths of the targets were chosen such that the rate of secondary beam particles in the spectrometer was comparable for the two beam polarities. The target was held in a target box made of ceramic plates with holes for the targets. The movement of the box was remotely controlled and depending on the polarity of the secondary beam particles to be selected, the corresponding target was moved into position. In all cases, the z position of the target was at -638.0 cm. The cross-section of the incident beam was elliptical with a horizontal full-width at half-maximum (FWHM) of 0.9 mm and a vertical FWHM of 1.2 mm at the target.

2.4 Collimator

Downstream of the target was a collimating channel which was positioned inside a 6.1 m long dipole magnet. The collimator was built from five blocks of brass and tungsten joined together as shown in Figure 2.1. The radius of curvature of the collimating channel was 270 m and the defining aperture was 0.5 cm × 1.0 cm. The secondary beam particles produced from the target were bent and steered into the collimator channel by the dipole magnet. The magnet produced a 1.67-T field which was monitored using Hall probes. To switch from negatively charged to positively charged secondaries, the polarity of the dipole magnet and the analysis magnets (Section 2.7) were reversed. Typically the secondary beam rate at the exit of the collimator was approximately 14 MHz.

E 871 Channel

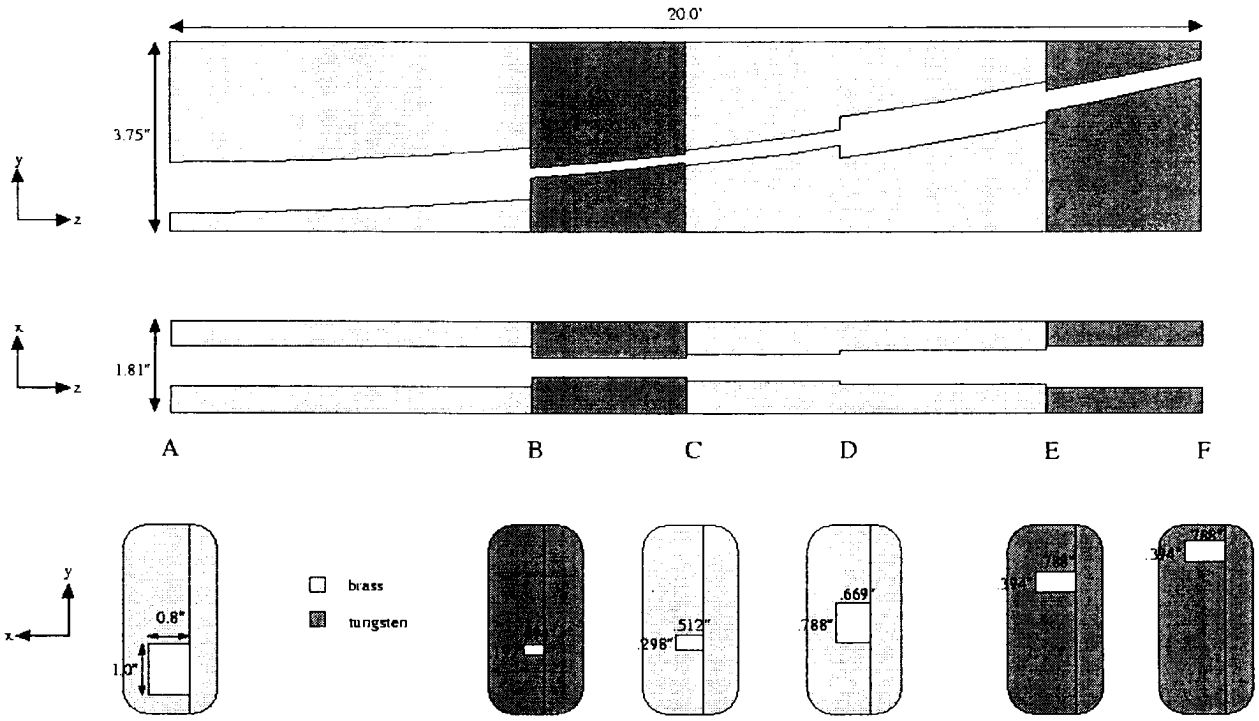

Bend angle = 19.5 mrad
Central orbit momentum = 150 GeV @ 1.6 T

Figure 2.1 The HyperCP hyperon channel

2.5 Decay Pipe

Immediately downstream of the collimator was an evacuated decay pipe 1300 cm long in which most of the secondary beam particles decayed. The volume was evacuated to eliminate interactions with matter and to avoid multiple scattering of the secondaries.

Figure 2.2 shows schematic representations of the elevation and plan views of the HyperCP spectrometer. The following sections will briefly describe the different elements of the spectrometer.

2.6 Wire Chambers

Given the high rate of hyperon decays HyperCP expected to record, the Multiwire Proportional Chambers (MWPCs) were designed to be fast, efficient, and capable of handling high rates. Downstream of the decay pipe were four high-rate MWPCs followed by a BM109 analysis magnet (described in Section 2.7), and downstream of the magnet were four more MWPCs, thus making up a total of eight (C1-C8) chambers. There was a ninth wire chamber which was used for testing and debugging and served as a spare.

All the wire chambers were similar in construction and had narrow wire spacings and small anode-cathode gaps. Each chamber was made of four anode planes sandwiched between cathode foils and two outer ground foils. The four anode wire plans correspond to the views X, X', U, and V. The X and X' bend-views are staggered by half a wire spacing, and the U and V stereo views were inclined at angles $\pm 26.6°$. The spacing between the wires ranged from approximately 1 mm (for C1 and C2) to 2.0 mm (for C7 and C8). As the particles traverse the spectrometer, they diverge from the secondary beam, and further, charged particles get bent by the analysis magnet. As a result, the lateral dimensions of the MWPCs progressively increased going downstream. Since in the upstream wire chambers the decay products are

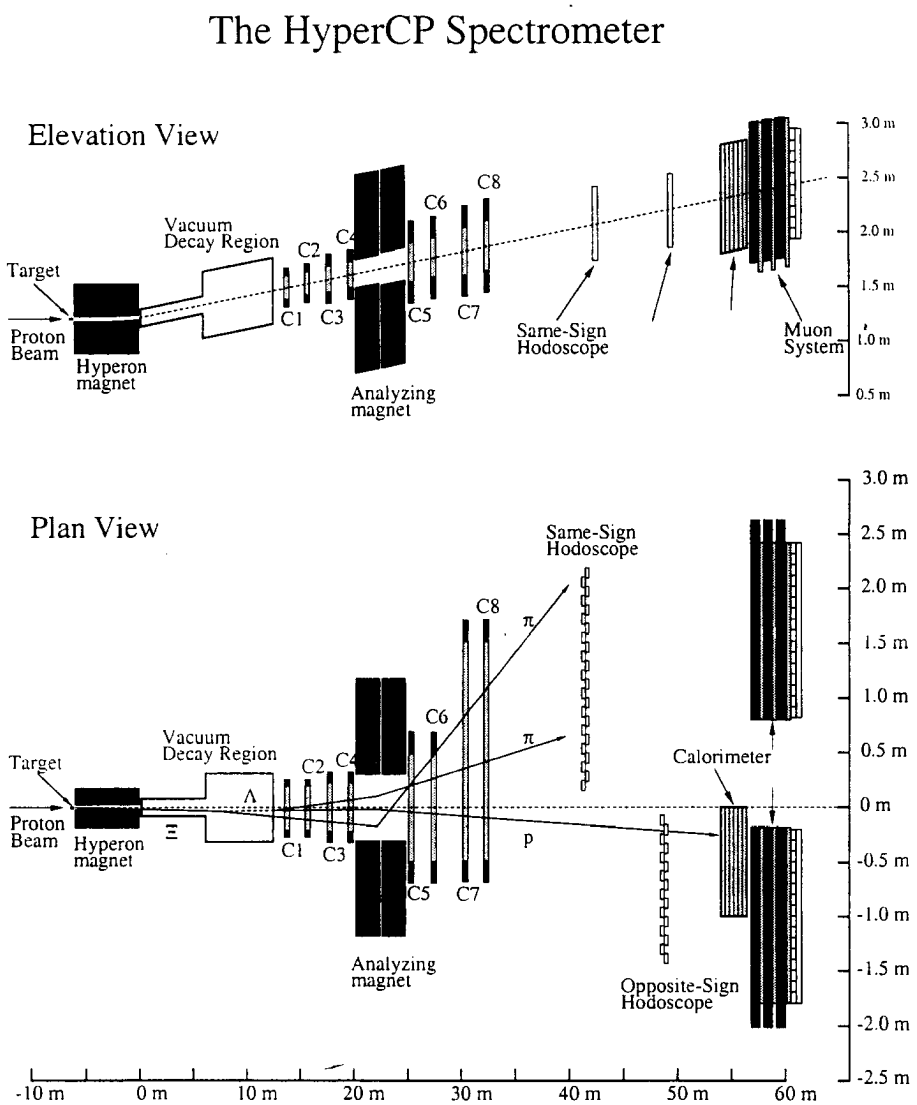

Figure 2.2 Elevation and Plan Views of the HyperCP Spectrometer

not well separated from the secondary beam, those chambers were filled with a fast gas mixture of CF_4-isobutane to reduce their sensitivity to out-of-time hits. The downstream chambers were filled with a mixture of Argon-Ethane-Isopropyl. The chambers were highly efficient ($\sim$ 99%), and almost no aging of the anode wires was observed over the course of the experiment.

2.7 Analysis Magnets

The analysis magnet used to steer charged particles from the decays was located between the two sets of MWPCs. The magnet consisted of two 228.6 cm long BM109 dipoles separated by 7.6 cm. The effective field length was 194.0 cm. The aperture of the upstream dipole magnet was 61 cm in x and 26 cm in y, while that of the downstream magnet was 61 cm $\times$ 30.5 cm. The magnetic field was directed in the y direction and the magnet was run at a current of 2500 A. The combined p_t kick to the transverse momentum was 1.43 GeV/c, such that the decay products were well separated from each other as well as from the secondary beam downstream of the magnet. This allowed for a simple trigger to be set up in the downstream segment of the spectrometer. The magnetic field in the central region of the magnet was quite uniform and was monitored on a spill-by-spill basis with two Hall probes placed near the middle of each magnet.

2.8 Hodoscopes

Two sets of hodoscope counters were used in the spectrometer. Each hodoscope station was made up of scintillation counters 9.0 cm wide, 66.0 cm high, and 2.0 cm thick. Each counter had an overlap of $\sim$1.3 cm with its neighbor. This was done in order to reduce inefficiencies in detection. Particles with positive and negative charges were bent in different directions by the analysis magnet. The set of hodoscope counters located on the side of the particles with the same charge as that of the secondary beam are referred to as same-sign (SS) hodoscopes, whereas the counters on the side of particles with charge opposite to the secondary beam are referred to as opposite-sign (OS) hodoscopes. In the spectrometer, the SS hodoscope station was made up of 24 counters, while 16 counters made up the OS hodoscopes.

2.9 Calorimeter

The calorimeter used in the experiment was a hadronic sampling calorimeter consisting of 64 layers of 0.5-cm-thick plastic scintillators sandwiched between 2.41 cm of iron. The total length of the calorimeter was 238.9 cm and the face was approximately 1 m square in area. The length corresponds to 9.6 interaction lengths (λ_I). Iron was chosen over lead as the absorber material because the critical energy of muons in iron is greater and thus energy losses due to muon bremsstrahlung are lower. The calorimeter was read out using wavelength shifting fibers embedded in keyhole-shaped grooves machined in the scintillator. The fibers were 2 m long and 2 mm in diameter and were read out at one end while the other was sputtered with aluminium. The readout ends were attached to a light guide coupled to a photomultiplier tube. The calorimeter was divided into 8 cells (2 rows of 4 cells each, in the transverse direction) with 256 fibers in each cell.

2.10 Muon System

On either side of the secondary beam channel, behind the calorimeter, was a muon detection system. The purpose of the muon detectors was to search for rare and forbidden decays such as $\Xi^- \to p\mu^-\mu^-$. The information from these detectors was not used for tracking or triggering on the primary Ξ^- decays, but was rather used in later stages of event selection and analysis. Each muon detector was made up of three stations (front, middle, and rear) of proportional tube chambers and a hodoscope. Steel blocks, approximately 185 cm wide, 150 cm high, and 75 cm thick separated the chambers from each other. The proportional tube chambers were filled with a mixture of 90% Argon-10% CO_2. Each station of proportional tubes consisted of vertical and horizontal views. The vertical view was used to measure the horizontal (x) position, while the horizontal view measured the position in the vertical (y) direction. In each station, the vertical tubes were located immediately behind the steel block and the horizontal tubes were located approximately 2 cm behind the vertical tubes. There were 64 vertical and 40 horizontal wires in each

station with a width of 1 inch. The hodoscopes were located about 10 cm behind the rear station of proportional tubes and were made up of scintillation counters crossed in the x and y directions. Each counter was approximately 10.2 cm wide and 102.0 cm high. 15 vertical counters and 10 horizontal counters made up the hodoscope. The hodoscope triggered on in-time muons.

2.11 Trigger

The triggers were designed to be fast and efficient and at the same time simple, in order to minimize biases. A total of 24 triggers were used. Most decays of interest shared a common feature: they have at least one particle track on the SS side of the spectrometer and another particle on the OS side. For this reason, a simple coincidence of particles in the OS and SS hodoscopes formed the basis of most of the physics triggers. In addition to a left-right coincidence between the hodoscopes, the proton from the decay $\Xi^- \to \Lambda\pi^-$, $\Lambda \to p\pi^-$ and the appropriately charged pion from the decay $K^\pm \to \pi^\mp\pi^\mp\pi^\pm$ deposited energy in the calorimeter. Hence, the cascade and kaon triggers (CAS and K), in addition to the left-right coincidence of particles in the hodoscopes, also required a certain minimum energy deposit in the calorimeter. The threshold energy for the CAS trigger was 70 GeV and it was 20 GeV for the K trigger. In addition to these main physics triggers, triggers for rare decays and monitoring studies were also implemented.

2.12 Data Acquisition System

The HyperCP data acquisition system (DAQ) [23] was built to be high-rate, efficient, and capable of high throughput. For events that satisfied at least one trigger the information from the various detector elements was read out and latched by two front-end electronic read-out systems. Digitized data from the MWPCs, trigger hodoscopes, and the calorimeter were latched using one system and signals from the muon proportional tubes and hodoscopes were handled by a second system. The data were carefully balanced in five paths, four for the MWPCs, hodoscopes and

calorimeter and one for data from the muon detector. Since the control room was about 160 m from the electronics hall the data were transmitted using five optical fibers. These optical signals were converted back to digital data and stored in five FIFO (first-in-first-out) event buffers each having 192 MB of memory. The events were stored in the buffers as the DAQ built events and wrote them to magnetic tapes. The event buffers served five 6U VME crates working in parallel. Each crate consisted of three Motorola MVME167 single-board central processing units (with 8 MB of memory on board), five Event Buffer Interfaces (EBI) and three SCSI interfaces functioning as magnetic tape controllers. In each crate, the first MVME167 CPU scheduled and monitored the event-building while the other two CPUs were responsible for building events from the five event fragments. Each event fragment was attached with an Event Synchronization Number (ESN) which was verified by the CPU building the event. The EBIs provided the interface between the MVME167 CPUs and the FIFO buffers. Each of the SCSI interfaces controlled three magnetic tape drives (EXB-8505) each capable of a maximum read-write rate of 500 KB/s in uncompressed mode. Thus, each crate had a maximum of nine tape drives that could record data. However, only eight drives in each crate were used at one time in the 1997 run.

The maximum trigger rate in the experiment was approximately 84 kHz while the typical rate of taking triggers was 63 kHz. At the maximum trigger rate the sustainable throughput of the DAQ was 16 MB/s with an average live time (fraction of generated triggers which are accepted) of about 65%. At the typical trigger rate of 63 kHz, the sustained DAQ throughput was 12 MB/s and the average live time was 75%.

What has been described so far is the fast DAQ which recorded events on tape. In addition, information such as beam positions, fields and temperatures of the magnets, and scalers were recorded on hard disks using a slow DAQ program based on the CAMAC protocol. Also, information from the detectors was monitored in real time using a monitoring program.

2.13 Summary Of Data Collected

HyperCP recorded data in runs lasting approximately six hours each. The average time it took to fill forty 5GB Exabyte tapes. Since the production cross-section of Ξ^- hyperons is more than twice that of $\overline{\Xi}^+$s, for every run recorded with a negatively charged secondary beam there were two runs with positive beam resulting in twice as much positive data as negative. Between April and September of 1997, a total of approximately 9,000 tapes were written corresponding to about 62 billion unpolarized events. In addition, data were taken with a polarized secondary beam, but these were not used in the present analysis.

CHAPTER III

DATA PROCESSING AND SELECTION

The data collected from the experiment were processed using an algorithm for reconstructing and selecting events. The following sections will describe the procedure for track-finding, the scheme used for processing the data, and the criteria for selecting events. The rules for selecting events for the present analysis are also described.

3.1 Track Finding

The positions of charged particles as they traversed the spectrometer were recorded by the MWPCs. As mentioned in Section 2.3, each MWPC had four plane views, X, X', U, and V. Thus, there were 32 measurements of the coordinates of each charged particle track. Since sometimes a particle could produce more than one hit, the algorithm clusters hits by combining adjacent hits on a plane and forming a single hit. This is done only for the four upstream MWPCs since downstream of the analysis magnets the tracks are fairly well separated. Based on hits in the four views within a MWPCs, a space-point – in other words, the x and y coordinates – of the track at that MWPC station was formed. While forming space-points, it was required that there be hits in at least three out of the four views. Once space-points were formed, upstream and downstream track segments were constructed by requiring at least two space-points for the successful formation of a segment. The track segments upstream and downstream of the analyzing magnet were then matched at the magnet's bend-plane. Selected tracks were labeled as SS, OS, or beam tracks depending on which side of the channel beam they lay on as explained in Section 2.8.

3.2 Data Reduction

Once tracks were found, events were selected into various "streams" for further processing. Since there are a variety of physics goals that could be pursued by the experiment, subsets containing data of interest for each topic were written to different streams. The selection criteria, while broad, still enabled significant reduction of the data. A brief description of the various streams is listed in Table 3.1. The selected events were written on Data Summary Tapes (DSTs) for further detailed analyses. It should be noted that streams 2 and 5 (3 and 6) have the same events, the difference between the two being in the format. Whereas an event on stream 2 (3) had a raw and a DST component to it, the same event on stream 5 (6) had only the DST portion. For the present analysis, data from stream 7 were used since the search involves muons in the final state. The requirements for an event to be selected for stream 7 were

I. the event must have ≥ 3 tracks.

II. at least one of the tracks must be identified as a muon track.

In the next section, the algorithm for selecting muons is described.

Table 3.1 Output Streams

Stream	Contents
2	$\Xi^{\pm}$,Ω
3	$K^{\pm} \rightarrow \pi^{\pm}\pi^{\pm}\pi^{\mp}$
4	K_s, prescaled triggers
5	$\Xi^{\pm}$,Ω
6	$K^{\pm} \rightarrow \pi^{\pm}\pi^{\pm}\pi^{\mp}$
7	μ
8	$\Lambda \rightarrow p\pi^{-}$
9	2 track events

3.3 Muon Selection

As mentioned in Section 3.2, events with at least one muon track were selected to be written to stream 7. A track was identified as a muon track in the following way:

I. Once a track was found, it was extrapolated to the location of the muon detector. At each view of a muon proportional tube station, if there was a hit in a wire ± 4.5 cm of the projected track position, the track was said to have a hit in that view at that station.

II. If the track had hits in the x and y views in two out of the three proportional tube stations, it was identified as a muon track.

The pitch of wires in the proportional tubes was 2.54 cm. Thus, requiring that there be a wire hit within 4.5 cm of the the projected track position was not a stringent requirement. Figure 3.1 shows the distributions of the absolute difference between the track projection and hits in the front muon proportional tube chamber. As can be seen, requiring that a track have a hit within ± 4.5 cm is a reasonable requirement and it also removes tracks which aren't well correlated with hits in the chamber views. Figure 3.2 shows the corresponding distribution for the x and y views of the muon hodoscope on the SS side. These requirements were refined and made tighter in a later stage of the analysis described in Section 3.6. The efficiencies of the muon proportional tubes were approximately 90% and the muon hodoscopes were $> 98\%$ efficient. Section 3.4 describes how the efficiencies were computed. Each event written to the output carried a tag known as "event type" to indicate the type of decay or particles associated with the event. An event with one identified muon track was tagged as being of type "muon" while an event with two muon tracks was tagged as "di-muon."

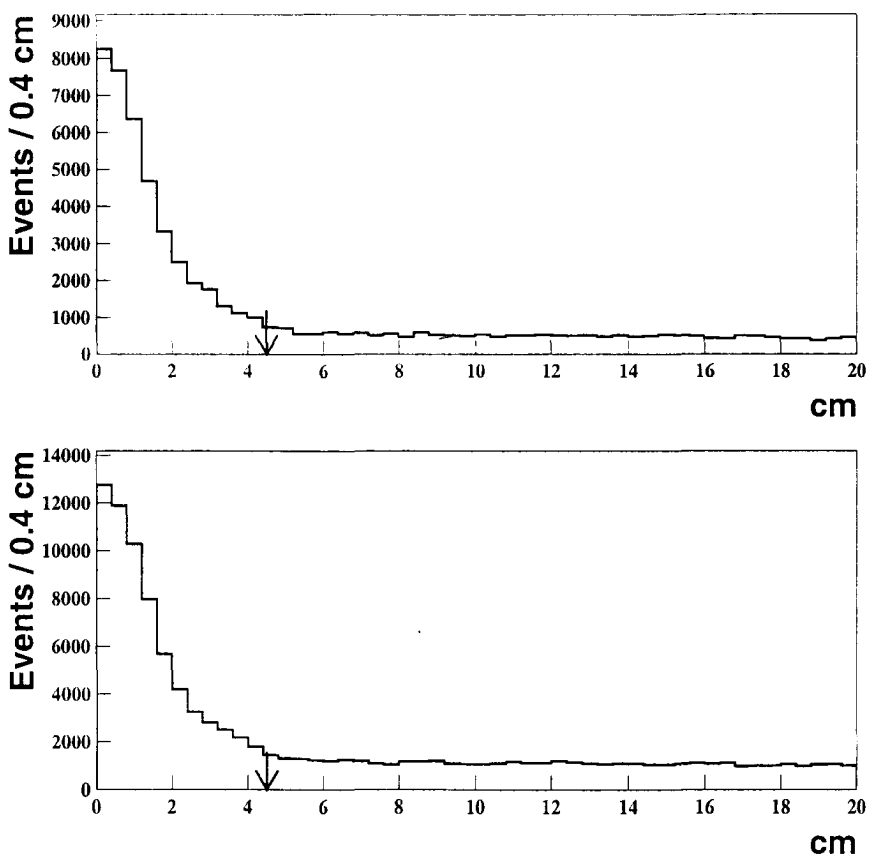

Figure 3.1 Absolute Difference between Projected Track Position and Proportional Tube Hits in the Front Muon Chamber. The Top Plot Shows the Distribution for the x View while the Bottom Plot is for the y view. Tracks With Hits Within 4.5 cm of the Projection are Accepted

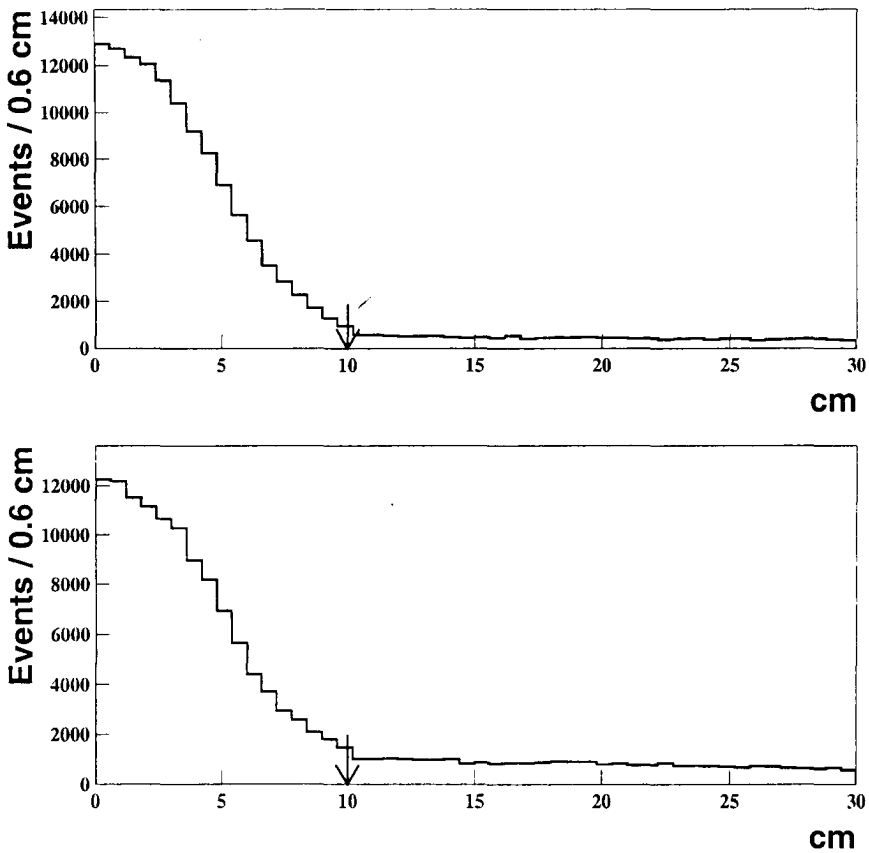

Figure 3.2 Absolute Difference between Projected Track position and Hodoscope Hits at the Muon Hodoscope. The Top Plot Shows the Distribution for the x view While the Bottom Plot Corresponds to the y View. The Arrows Indicate the Cut Location

3.4 Muon Detector Efficiencies

Since the present analysis involves only μ^- the efficiencies of the muon proportional tubes and the muon hodoscopes on the SS side were calculated. The efficiencies of the proportional tubes were calculated in the following way: A track was required to have hits in both the x and y views of the muon hodoscope by aiming the track at the hodoscopes and requiring a hit within $\pm$ 10 cm of the track in each view. The sample thus selected was then used to determine the individual efficiencies of the muon chambers. As explained in Section 2.10, the muon detector had three stations of proportional tube chambers with x and y readout views for each chamber. To determine the efficiency of the front muon chamber, it was required that the track have hits in x and y views in the middle and rear chambers. Then, the ratio of the number of tracks with x and y hits in all three chambers to the number of tracks with x and y hits in only the middle and rear chambers gives the efficiency of the front chamber. It should be noted that this is the efficiency of the front chamber for both x and y views. The efficiencies for the middle and rear chambers were determined in a similar fashion. The efficiencies were determined to be 86.2%, 90.7%, and 87.3% for the front, middle, and rear chambers respectively.

To determine the efficiency of the muon hodoscope, a similar technique was used, but instead of selecting a sample by requiring hits in the hodoscopes, it was required that the tracks have hits in the x and y views of all three muon chambers. In this sample, the efficiency of the x view, for example, was calculated from the ratio of number of tracks with hits in both x and y views to the number of tracks with a hit in the y view. The hodoscope efficiencies were thus determined to be 98.8% and 98.6% for the x and y views. These efficiencies were used in the calculation of the muon selection efficiency and, in turn, the branching ratio for the decay $\Xi^- \to p\mu^-\mu^-$ as described later in Section 4.6. Systematic studies of the variation in muon chamber and hodoscope efficiencies are described in Section 4.3.

3.5 DST Production

Approximately 10,000 raw data tapes were processed at Fermilab on a farm of CPUs using the algorithm described above. Tapes were mounted on a central node and each tape was then split into 10 approximately equal files. The files were shared across the network to 35 processing nodes. Each node could process four files at a given time (two per CPU) and the output of the processing (reconstruction and event selection) was written to a local disk on the processing node. There were 8 output files on disk (one per stream) for each input file. Thus for each raw data tape there were 80 output files. These files were then collected and copied back to the central node. In order to avoid mixing output streams, specific areas on disk were allocated for each stream and the outputs were copied back to the appropriate area. Once the disk holding an output stream was close to being full, its contents were concatenated and written to DSTs. The entire process was managed by a set of scripts that communicated with Fermilab Farms Batch System software (FBS) [24].

50 stream-7 DSTs (17 for negative data and 33 for positive data) were produced from the processing of unpolarized data from HyperCP's run in 1997. These DSTs were then analyzed in more detail and the search for $\Xi^- \to p\mu^-\mu^-$ was performed on this data set as described in the following sections and Chapter 4. The information stored for each event is listed below. In addition to a DST block, each event on the stream-7 output tapes also contained the raw data component. The size of a DST block was 150 bytes and the raw data component was approximately 600 bytes. Thus each 5 GB stream-7 DST contained approximately 7 million events.

I. Event type

II. Number of SS tracks

III. Number of OS tracks

IV. z of bend-plane

V. $\int B \cdot dl$

VI. Encoded proportional tube and hodoscope hits (for each track)

VII. Slopes (for each track)

VIII. Intercepts (for each track)

IX. Compressed raw hits in MWPCs

X. Trigger information

3.6 Final Selection Cuts

A detailed search for the decay $\Xi^- \rightarrow p\mu^-\mu^-$ was performed on a set of 17 stream 7 DSTs. The criteria for the preliminary selection of events to stream 7 were rather loose in order to not reject any potential muon candidate tracks. A significant fraction of the events on the tapes were expected to be from the decays of Ξ^- and K^- where pions from the decays $\Xi^- \rightarrow \Lambda\pi^-$, $\Lambda \rightarrow p\pi^-$, and $K^- \rightarrow \pi^-\pi^-\pi^+$ were misidentified as muons. Pions from these and other decays could punch through the muon detector steel and result in hits in the muon proportional tubes and hodoscopes. In addition, pions could decay in flight and the resulting muon from the decay $\pi^- \rightarrow \mu^-\bar{\nu_\mu}$ would produce hits in the muon detectors. Approximately 6×10^8 Ξ^- and 3×10^8 K^- were expected to be reconstructed by the experiment which would lead to significant background in the search for $\Xi^- \rightarrow p\mu^-\mu^-$. Other sources of background are expected from particle interactions with the material in the spectrometer, accidental tracks, and misreconstruction of tracks leading to "ghosts" or fake tracks. In order to minimize background events and enhance any possible signal from the decay $\Xi^- \rightarrow p\mu^-\mu^-$ a set of selection rules were imposed on the data.

In devising the rules, the locations of the cuts were determined based on $\Xi^- \rightarrow \Lambda\pi^-$, $\Lambda \rightarrow p\pi^-$and $K^- \rightarrow \pi^-\pi^-\pi^+$ background events in order to minimize biases in the cuts and also to ensure the cuts were efficient and optimized for minimizing potential backgrounds.

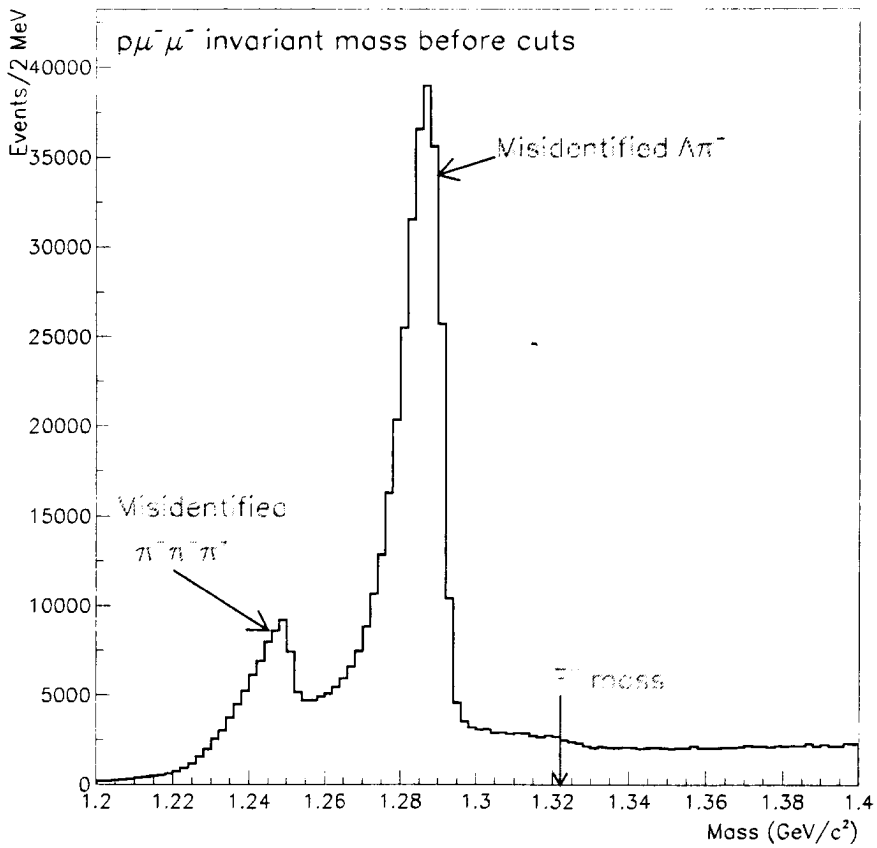

Figure 3.3 Invariant $p\mu^-\mu^-$ Mass Distribution for Three-track Events in Stream-7 Before Applying Any Cuts

I. Di-muon selection

When tracks were identified as muons during selection for stream 7, the information in the muon hodoscopes was not used. Thus the tracks could be out of time and not have corresponding hits in the hodoscope counters. For this reason, it was required that each muon track also have correlated hits in both the x and y views of a hodoscope counter. This was done by projecting the track back to the hodoscope station and requiring that there be a hit within $\pm$ 10 cm of the projected position of the track. As mentioned earlier, the width of each hodoscope counter was 10.16 cm.

II. Ξ^- momentum

Figure 3.4 shows the distribution of the Ξ^- momentum accepted by the spectrometer. The reconstructed mean momentum was slightly larger than the design value of 160.0 GeV/c due to the target not being exactly centered at the collimator aperture. It was required that the momentum be between 125 GeV/c and 250 GeV/c.

III. OS momentum fraction

Kinematic considerations dictate that the momentum carried by the OS track is different for $\Xi^- \to p\mu^-\mu^-$ and $K^- \to \pi^-\pi^-\pi^+$ decays. The proton in the former decay carries a significantly larger fraction of the total momentum than the π^+ in the latter decay.

Figure 3.5 shows the distribution of the proton and the π^+ momenta from the decays $\Xi^- \to \Lambda\pi^-$ and $K^- \to \pi^-\pi^-\pi^+$ respectively. The distributions are fairly distinct and separated which makes it possible to impose a cut that will reject decays of the kaon while keeping Ξ^- decays. It was required that the momentum fraction of the OS track be > 0.6.

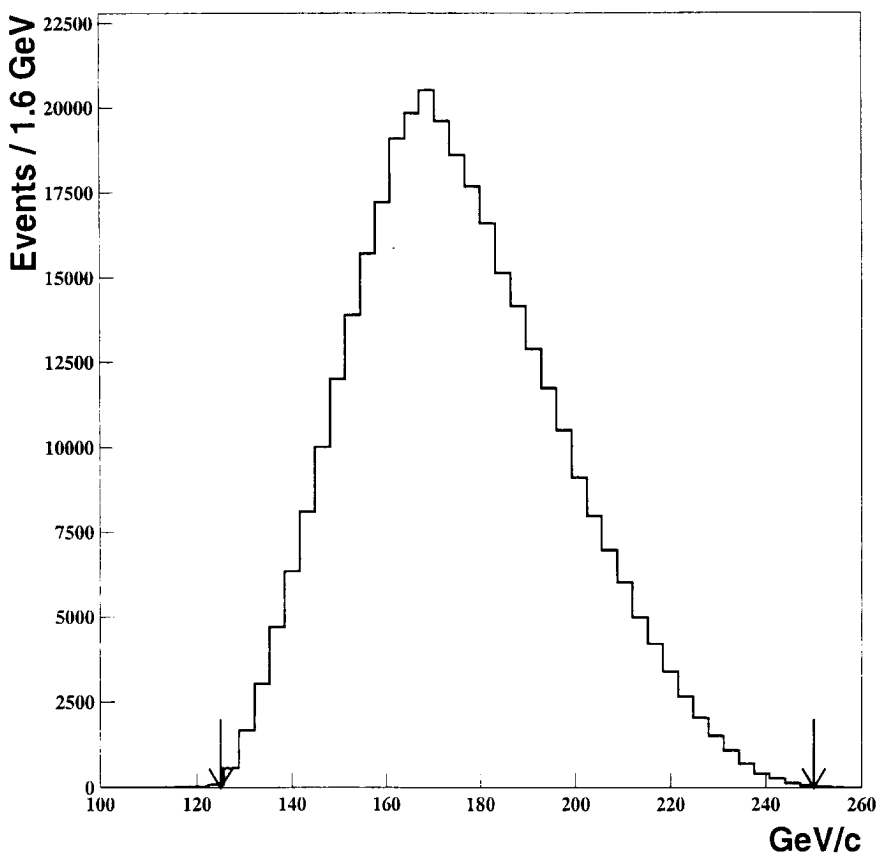

Figure 3.4 Distribution of Total Ξ^- Momentum. The Arrows Indicate the Limits of the Momentum Range Accepted

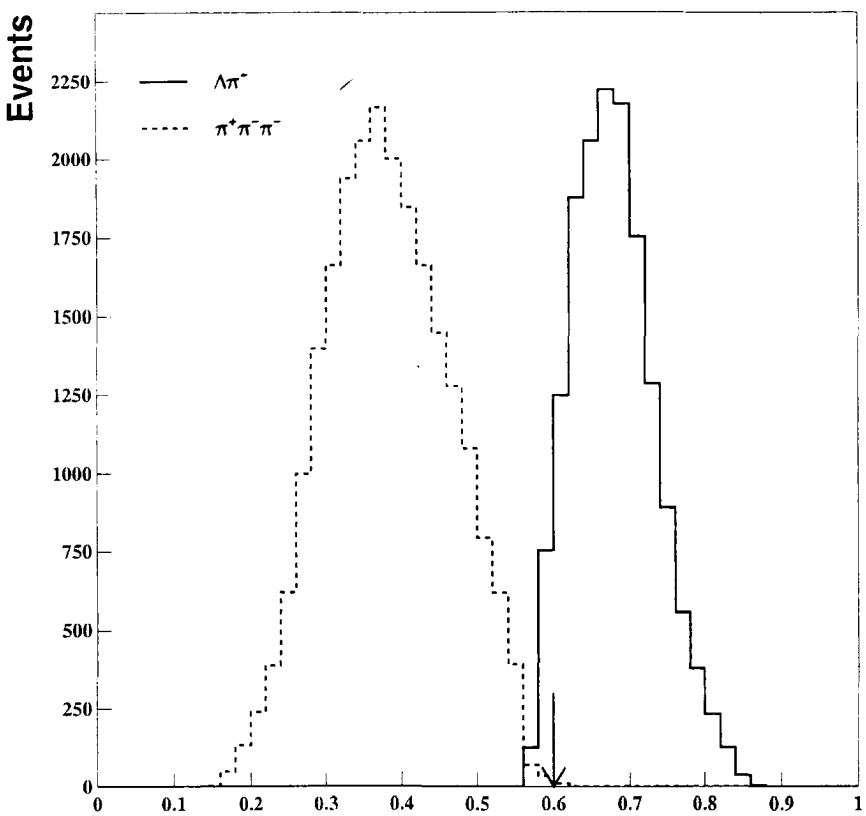

Figure 3.5 Momentum of the OS Track as a fraction of the Total Momentum for $\Xi^- \to \Lambda\pi^-$ and $K^- \to \pi^-\pi^-\pi^+$ Decays. The OS Track in the Decay $\Xi^- \to \Lambda\pi^-$, $\Lambda \to p\pi^-$ is a Proton and that in the Decay $K^- \to \pi^-\pi^-\pi^+$ is a Pion. The Arrow Indicates the Location of the Cut

IV. Reconstructed $p\pi^-$ mass

Assigning the mass of a pion to an SS track and the mass of a proton to an OS track, the invariant $p\pi^-$ mass was calculated. Since there are 2 SS tracks, the invariant mass was computed for both combinations of SS and OS tracks. If either resultant invariant mass was consistent with the mass of a Λ – between 1.1 GeV/c^2 and 1.125 GeV/c^2 – the event was rejected.

V. Reconstructed $\Lambda\pi^-$ mass

In addition to the above cut, events which satisfy a $p\pi^-\pi^-$ hypothesis were rejected. Figure 3.6 shows the reconstructed $p\pi^-\pi^-$ invariant mass for stream 7 events with 3 or more tracks. It was required that the $p\pi^-\pi^-$ mass be outside the range 1.315 - 1.330 GeV/c^2. This is a range of 7σ around the mean $\Lambda\pi^-$ invariant mass.

VI. Reconstructed $\pi^-\pi^-\pi^+$ mass

In order to reject pions from the decay $K^- \rightarrow \pi^-\pi^-\pi^+$, a cut was imposed on the $\pi^-\pi^-\pi^+$ invariant mass. Figure 3.7 shows the reconstructed invariant mass distribution under this hypothesis. Events within 10 MeV/c^2 of the K^- mass of 494.0 MeV/c^2 were thus excluded.

VII. Decay vertex

Figure 3.8 shows the distribution of the z position of the Ξ^- decay vertex. The exit window of the vacuum decay pipe is at $z = 1300.0$ cm, and the entrance is at $z = 0.0$. In order to exclude interactions with the material at the entrance and exit of the decay channel, it was required that the z of the decay vertex be between 50.0 cm and 1250.0 cm. It should be noted that in the case of the decays $\Xi^- \rightarrow \Lambda\pi^-$, $\Lambda \rightarrow p\pi^-$ this requirement was imposed on the decay vertex of the parent hyperon and the daughter baryon was allowed to decay downstream of the vacuum pipe.

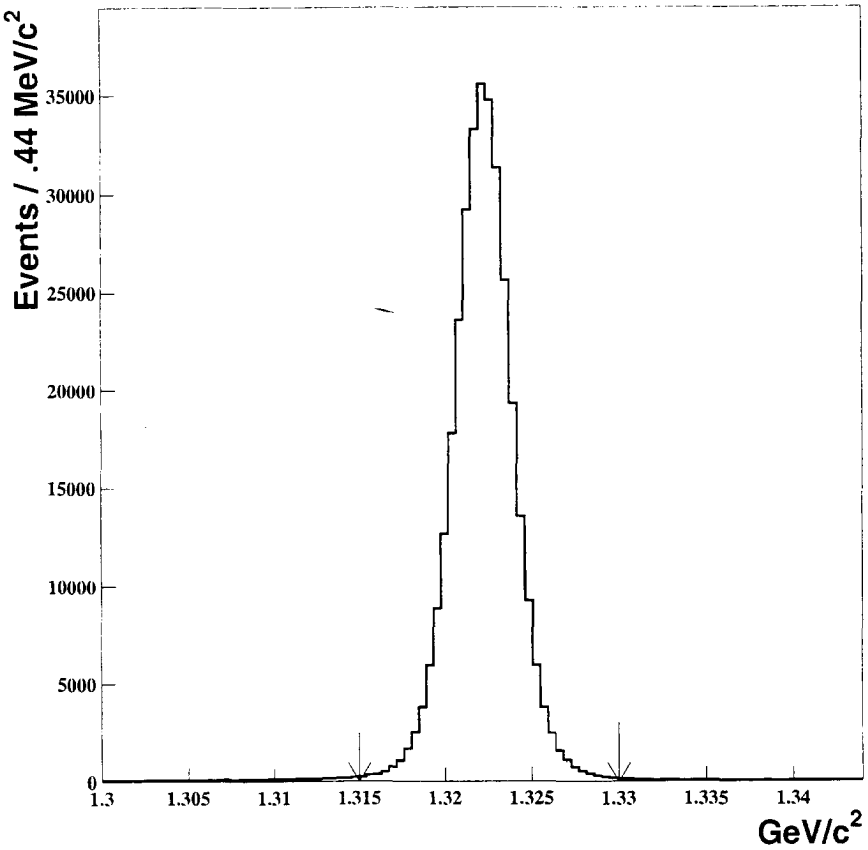

Figure 3.6 Distribution of the Reconstructed $\Lambda\pi^-$ Invariant Mass. Events with an Invariant Mass Between 1.315 and 1.33 GeV/c^2 are Excluded

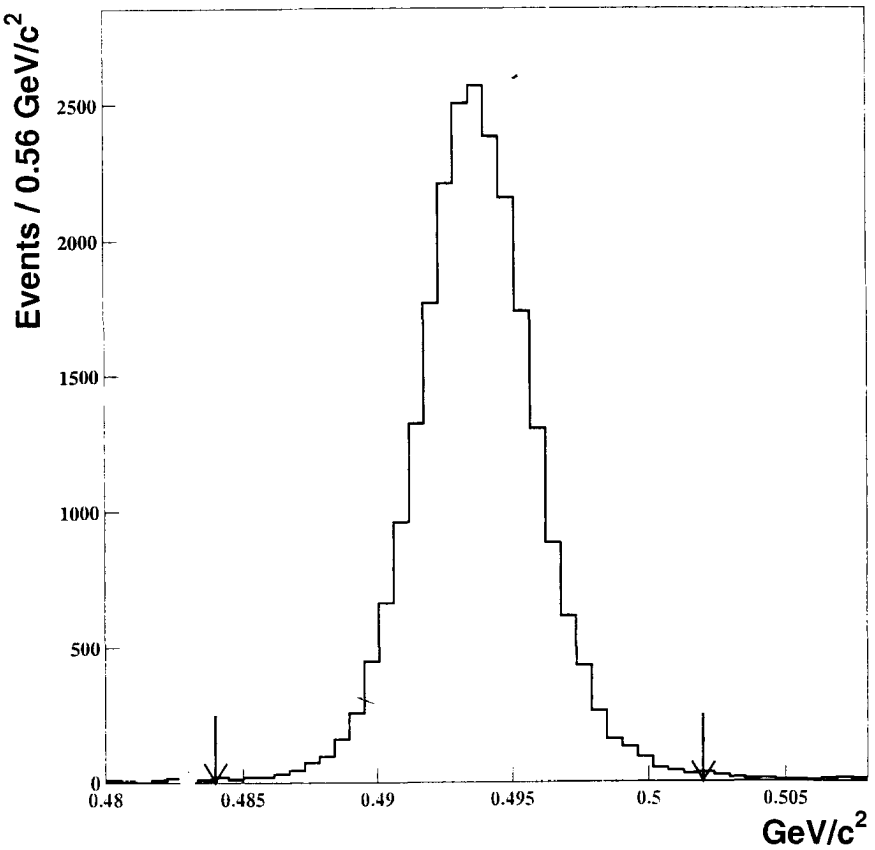

Figure 3.7 Distribution of the Reconstructed $\pi^-\pi^-\pi^+$ Invariant Mass. Events with an Invariant Mass Between 0.484 and 0.502 GeV/c^2 are Excluded. The Mean of the Distribution is at 0.494 GeV/c^2

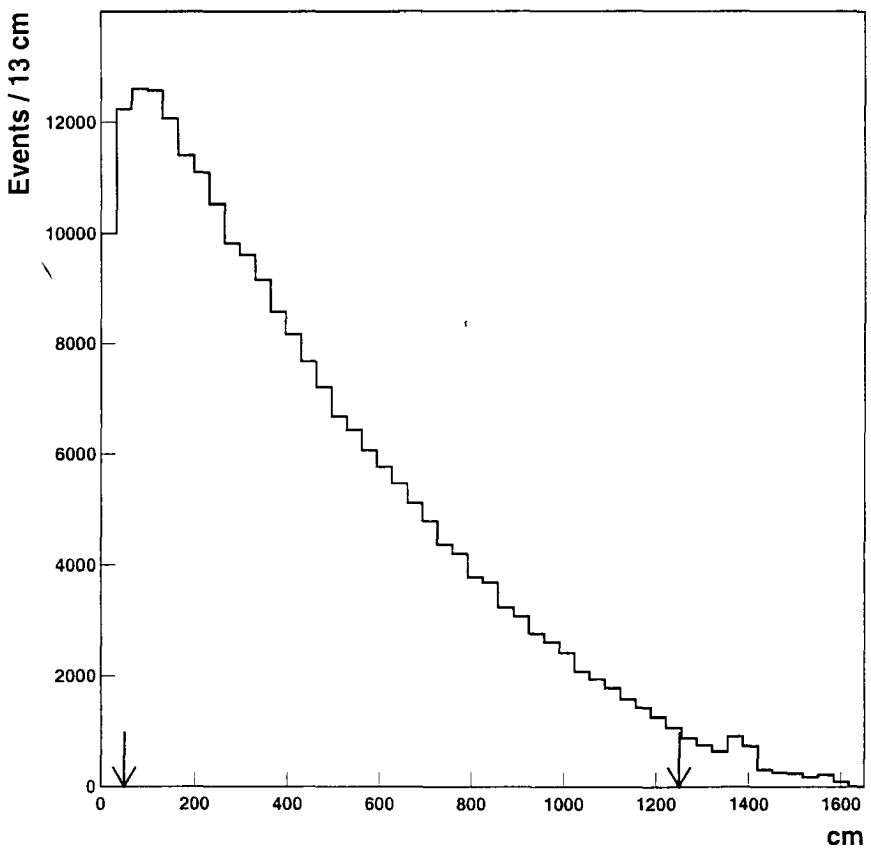

Figure 3.8 Distribution of the z Position of the Decay Vertex for $\Xi^{-} \to \Lambda\pi^{-}$ Decays. Accepted Events are between 50.0 and 1250.0 cm as Indicated by the Arrows. The Entrance and Exit of the Decay Pipe were at 0.0 and 1300.0 cm

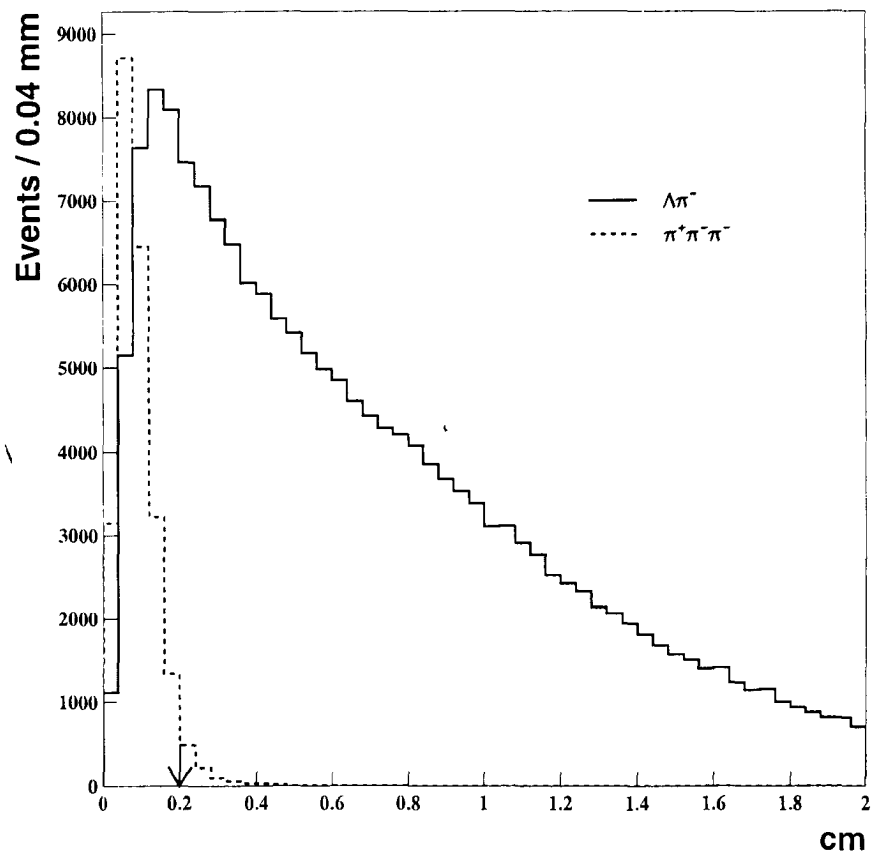

Figure 3.9 Average Distance between Tracks at the z of the Decay Vertex for $\Xi^- \rightarrow \Lambda\pi^-$ and $K^- \rightarrow \pi^-\pi^-\pi^+$ Decays. The Arrow Indicates the Location of the Cut. Note the Narrower Distribution for $K^- \rightarrow \pi^-\pi^-\pi^+$ – a Single-vertex Decay Topology

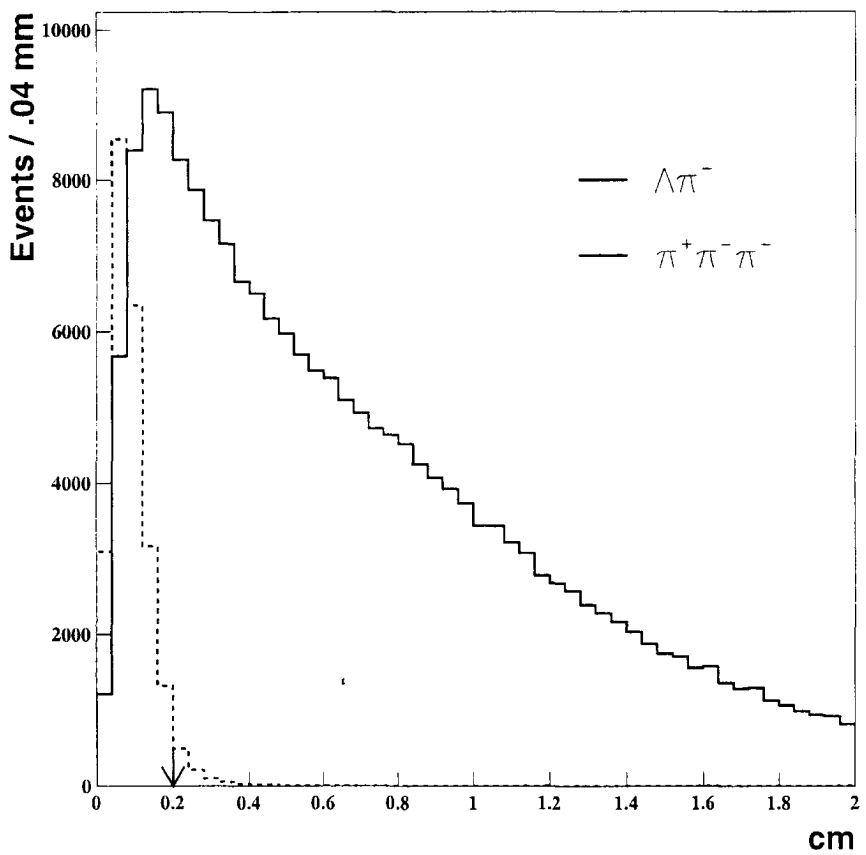

Figure 3.10 $\chi^2/ndof$ from Single-vertex Fit for $\Xi^- \to \Lambda\pi^-$ and $K^- \to \pi^-\pi^-\pi^+$ Decays. The Arrow Indicates the Location of the Cut

VIII. Single-vertex constraint

The decay $\Xi^- \to p\mu^-\mu^-$ is a three-body decay from a single vertex. This is in contrast to the decay chain $\Xi^- \to \Lambda\pi^-$, $\Lambda \to p\pi^-$ which has a primary and a secondary vertex. Requiring that the topology of events be consistent with decay from a single vertex is an additional means to reject background from $\Xi^- \to \Lambda\pi^-$ events. First, the decay vertex was found using the distance of closest approach method. The $\chi^2/ndof$ (χ^2 per degree of freedom) from fitting the tracks to the vertex and the average distance between tracks at the vertex were then used to discriminate between single-vertex decays from those of a different topology. In performing the fit, only hits in the upstream MWPCs were used. Figure 3.9 shows the distribution of the average distance between tracks at the decay vertex for $\Xi^- \to \Lambda\pi^-$ and $K^- \to \pi^-\pi^-\pi^+$ decays. The decay $K^- \to \pi^-\pi^-\pi^+$ is a single-vertex decay and hence of a topology similar to the decay $\Xi^- \to p\mu^-\mu^-$. As can be seen in Figure 3.9, the distributions are radically different for the two decays, which enables us to impose a cut that would reject background events from $\Xi^- \to \Lambda\pi^-$ and other decays not consistent with a single decay vertex. It was required that the average distance between the three tracks at the z of the decay vertex be < 0.2 cm. Figure 3.10 shows the distribution of $\chi^2/ndof$ from the single-vertex fit for $\Xi^- \to \Lambda\pi^-$ and $K^- \to \pi^-\pi^-\pi^+$ decays. It was required that this parameter be < 2.5 for an event to be accepted as being from a single-vertex decay.

IX. Target-pointing

In order to reject events coming from interactions of the secondary beam with material in the spectrometer, a target-pointing cut was applied. The Ξ^- track was traced back to the target location and the event was rejected if it didn't point back to the target. Figures 3.11 and 3.12 show the distributions of the x and y positions of the track at the z of the target. It was required that $\mid x \mid < 0.5$ cm and $\mid y - 6.55 \mid < 0.5$ cm. The distribution of the y position at the target is centered at 6.55 instead of at 0.0 because the co-ordinate system used for tracing the particle back to the target is defined relative to the central

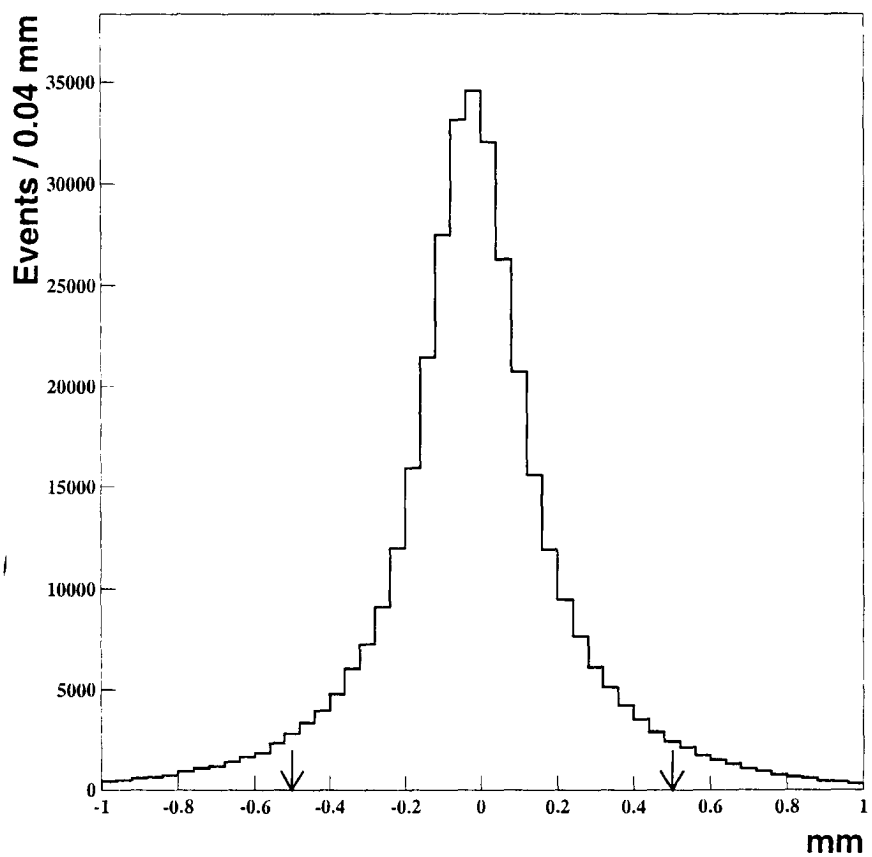

Figure 3.11 Projected x Position of Ξ^- at the Target

orbit that the channel beam traces through the collimating channel. Since the beam curves up (in y), there is an offset when defining the y position at the target. It should be noted that this is merely a convention and does not affect the actual kinematics or geometry of the particle.

X. Fake tracks

During track-finding, a single track was occasionally misinterpreted as two tracks due to ambiguous assignment of MWPC hits to track segments. This resulted in two copies of the same track, called "ghosts." A cut was made to rid the data of such tracks. The cut was based on differences in the the slopes and intercepts between the two tracks. Since it was initially required that there be only one OS track, this cut was necessary only for the SS tracks. The differences in slopes and intercepts translates to the requirement that the tracks be separated by > 0.5 cm at the location of the first muon chamber.

XI. Reconstructed $p\mu^-\mu^-$ mass

In addition to the above cuts, it was required that the reconstructed mass of $p\mu^-\mu^-$ candidates be in the range 1.315 – 1.33 GeV/c^2. From Monte Carlo simulation of the decay $\Xi^- \rightarrow p\mu^-\mu^-$(described in Section 4.1) it was estimated that the $p\mu^-\mu^-$ invariant mass distribution would have a width of approximately 2 MeV/c^2, which is similar to the width of the $\Lambda\pi^-$ invariant mass distribution. Thus the requirement imposed on the $p\mu^-\mu^-$ mass is equivalent to asking that the events be within 7σ around the mean Ξ^- mass.

Table 3.2 summarizes the selection criteria used in the present analysis. The cumulative effect of the cuts is shown in Table 3.3.

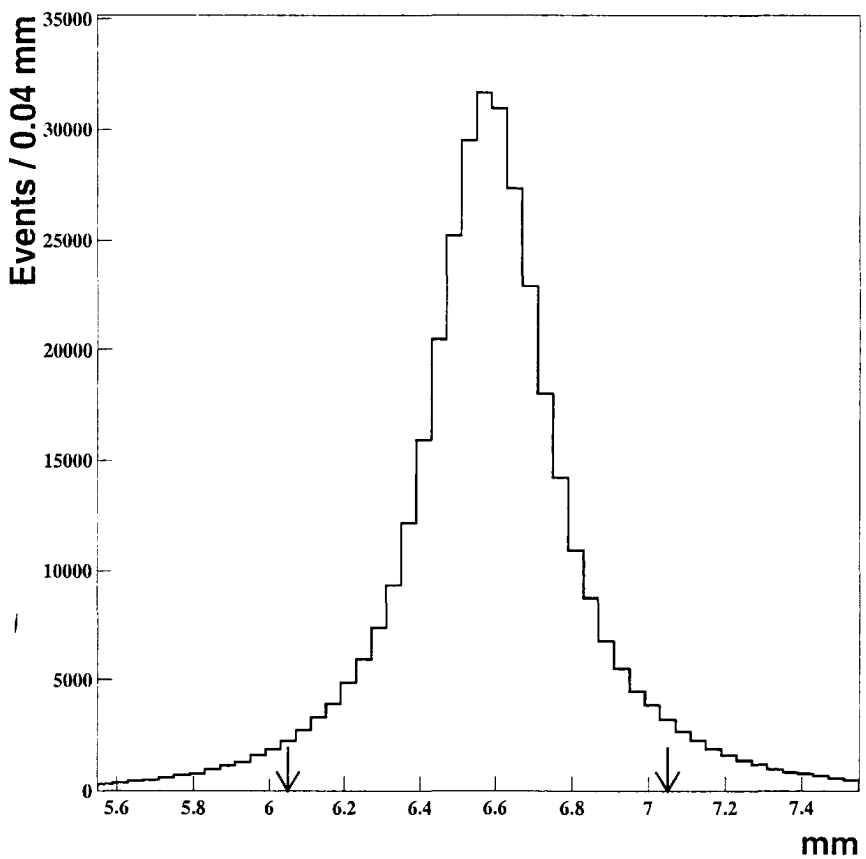

Figure 3.12 Projected y Position of the Ξ^- at the Target

Table 3.2 Summary of Selection Cuts

Cut parameter	Selection rule
Track multiplicity	accept 3 tracks, 1 OS + 2 SS
Ξ^- momentum	accept 125.0 GeV/c < 250.0 GeV/c
Momentum fraction of OS track	accept $\frac{p_{OS}}{p_{tot}} > 0.6$
$\Lambda\pi^-$ invariant mass	exclude $1.315 < m_{\Lambda\pi^-} < 1.33$ GeV/c^2
$p\pi^-$ invariant mass	exclude $1.1 < m_{p\pi^-} < 1.125$ GeV/c^2
$\pi^+\pi^-\pi^-$ invariant mass	exclude $0.484 < m_{\pi^+\pi^-\pi^-} < 0.502$ GeV/c^2
z of decay vertex	accept $50.0 < z < 1250.0$ cm
Avg. distance between tracks at decay vertex	accept $dist < 0.2$ cm
x position at z of the target	accept $\mid x \mid < 0.5$ cm
y position at z of the target	accept $\mid y - 6.55 \mid < 0.5$ cm
	exclude ghost tracks

Table 3.3 Efficiency of Selection Cuts

Cut	% Surviving after cut
Ξ^- momentum	92.73
Momentum fraction of OS track	78.66
$p\pi^-$ invariant mass	5.83
$\Lambda\pi^-$ invariant mass	5.04
$\pi^+\pi^-\pi^-$ invariant mass	5.01
z of decay vertex	3.31
Single vertex constraint	0.83
x, y at target	0.14
ghost tracks	0.11

CHAPTER IV

ANALYSIS II

The following sections will describe studies on background, estimation of geometric acceptance, and systematic effects.

The selection cuts described in the previous chapter were applied to all stream-7 data. To quantify the result from the application of these cuts, it is essential to know the flux of Ξ^- hyperons in the experiment, since the decay $\Xi^- \to p\mu^-\mu^-$ will be normalized to the dominant decay $\Xi^- \to \Lambda\pi^-$, $\Lambda \to p\pi^-$. This was done using a Monte Carlo simulation of the decay in the spectrometer and will be described shortly. Apart from helping calculate the flux the Monte Carlo was also used to study potential sources of background to the $\Xi^- \to p\mu^-\mu^-$ decay, efficiencies of the selection cuts for accepting signal events while rejecting background, and systematic uncertainties in the analysis.

4.1 Monte Carlo

Ξ^- hyperons were generated at the target using a simplified production model described later, and transported through the collimating channel. Since there is no known decay mechanism for the $\Delta L = 2$, $\Xi^- \to p\mu^-\mu^-$ in the Standard Model, it was modeled as a uniform three-body decay, while $\Xi^- \to \Lambda\pi^-$and $\Lambda \to p\pi^-$decays were generated as two-body decays. The daughter particles from the Ξ^- and Λ decays were then transported through the simulated spectrometer with multiple-scattering effects, interactions with spectrometer material, and detector efficiencies incorporated.

In the simple model used to produce Ξ^- hyperons at the target, the invariant production cross-section of the parent particle was assumed to be proportional to $e^{-p_T{}^2/a}(1-x_F{}^n)$ where p_T is the transverse momentum of the hyperon, x_F is Feynman x (the ratio of the longitudinal momentum of the hyperon to the total momentum, in

the centre of mass system of the proton beam), and a and n are tunable parameters dependent on the production kinematics.

It should be noted that Ξ^-s were produced in an identical manner for both $\Xi^- \to p\mu^-\mu^-$, and the normalization $\Xi^- \to \Lambda\pi^-$, $\Lambda \to p\pi^-$modes. Thus any systematic effects in secondary beam production at the target should show up in both the signal and the normalizing modes and should thus have no effect on the relative acceptance between the two modes. To verify that this is indeed the case we performed systematic studies by varying the tunable parameters in the production model and studying the resulting variation in the relative acceptance between the signal and normalizing decay modes. Detailed comparisons between simulated MC events and data taken by the experiment are described in Section 4.2.

Figures 4.1– 4.4 show invariant mass distributions from Monte Carlo simulations of the $\Xi^- \to p\mu^-\mu^-$ decay. The $p\mu^-\mu^-$ invariant mass distribution is shown in Figure 4.1. The width of the distribution was determined (Figure 4.2) to be 1.8 MeV/c^2. Figure 4.3 shows the distribution of $\Xi^- \to p\mu^-\mu^-$ decays reconstructed under the $\Lambda\pi^-$ hypothesis. As can be seen events with a reconstructed $p\pi^-\pi^-$ mass > 1.345 GeV/c^2 can be excluded without cutting into the signal region. The invariant mass distribution for $p\mu^-\mu^-$ events reconstructed under a $\pi^+\pi^-\pi^-$ hypothesis is shown in Figure 4.4. Figures 4.5– 4.9 show Monte Carlo distributions of parameters that were selected on in the analysis. The locations of the cuts have been described in Chapter 3. As mentioned earlier, efficiencies for the various cuts were determined from the simulation and a summary of these efficiencies is presented in Table 4.1.

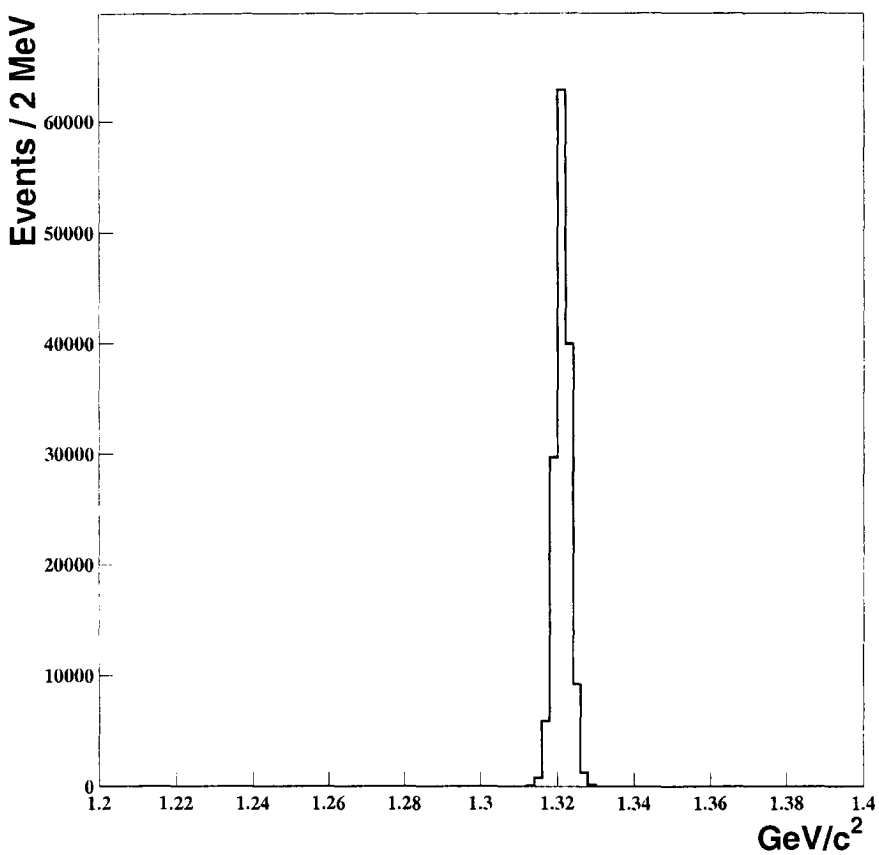

Figure 4.1 Invariant $p\mu^-\mu^-$ Mass Distribution from a Monte Carlo Simulation of the Decay.

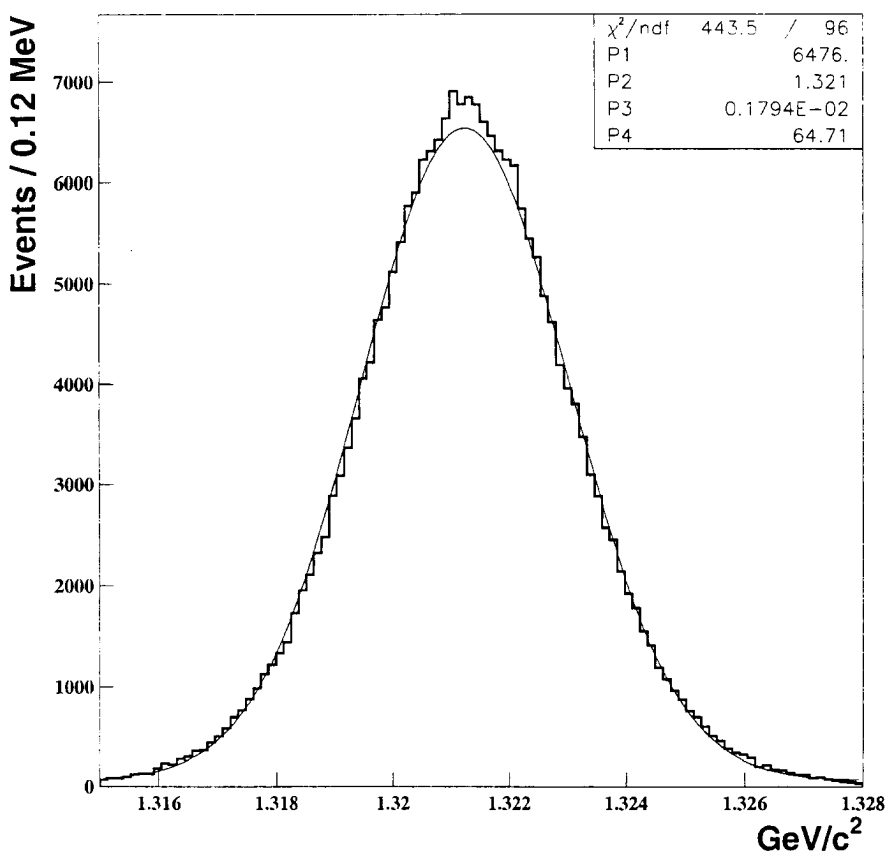

Figure 4.2 Invariant $p\mu^-\mu^-$ Mass Distribution and a Fit to the Distribution from Monte Carlo Simulation

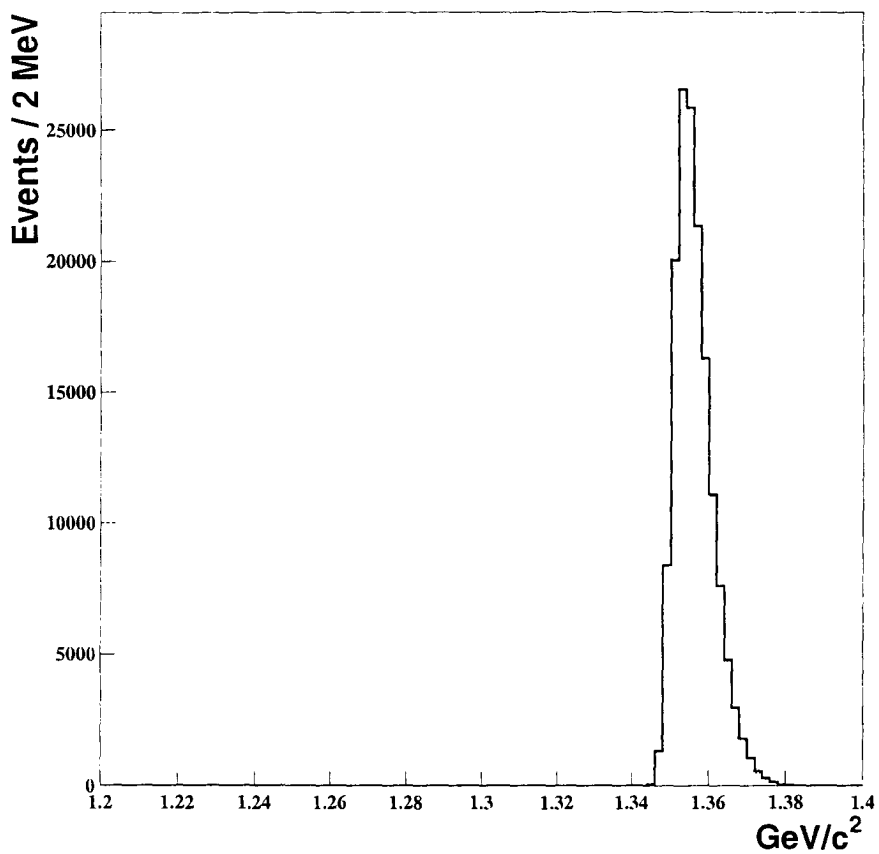

Figure 4.3 Monte Carlo Generated $p\mu^-\mu^-$ Decays Reconstructed as $p\pi^-\pi-$. Note the Distribution is Well Separated from the Ξ^- Mass of 1.321 GeV/c^2.

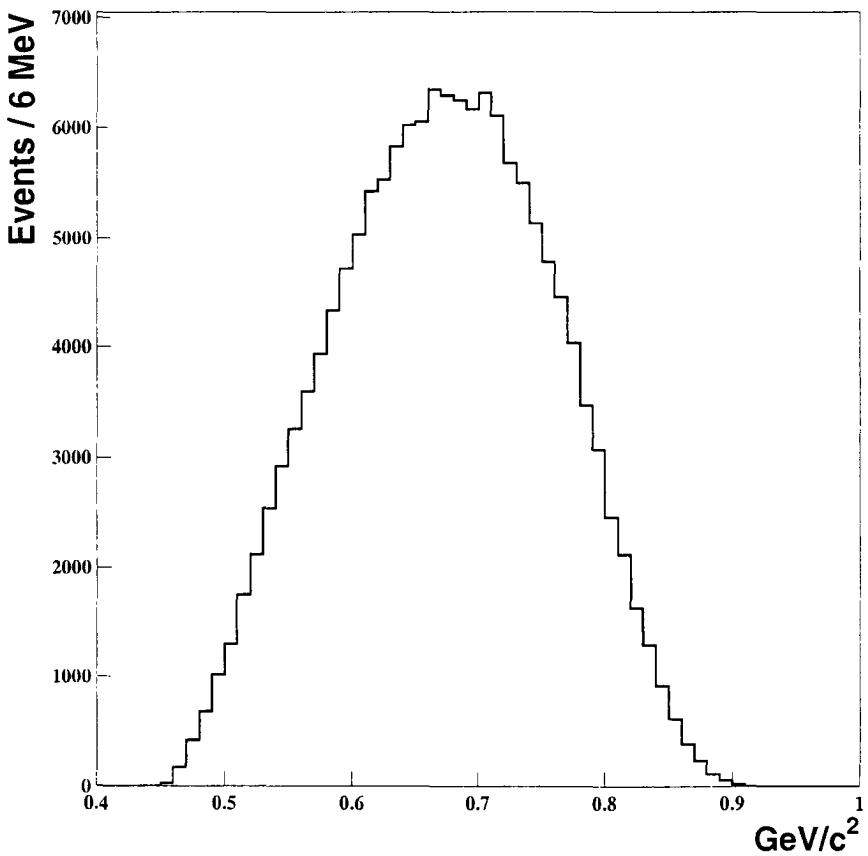

Figure 4.4 Monte Carlo Generated $p\mu^-\mu^-$ Decays Reconstructed as $\pi^+\pi^-\pi^-$ Events

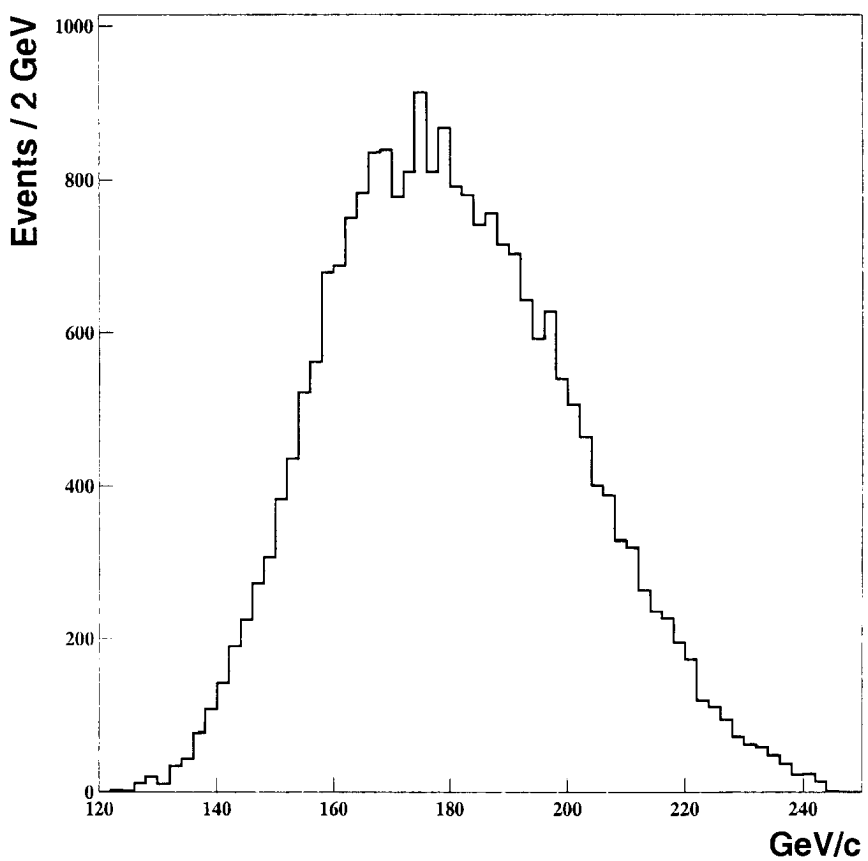

Figure 4.5 MC Distribution of p_{total} for $\Xi^- \to p\mu^-\mu^-$ Events

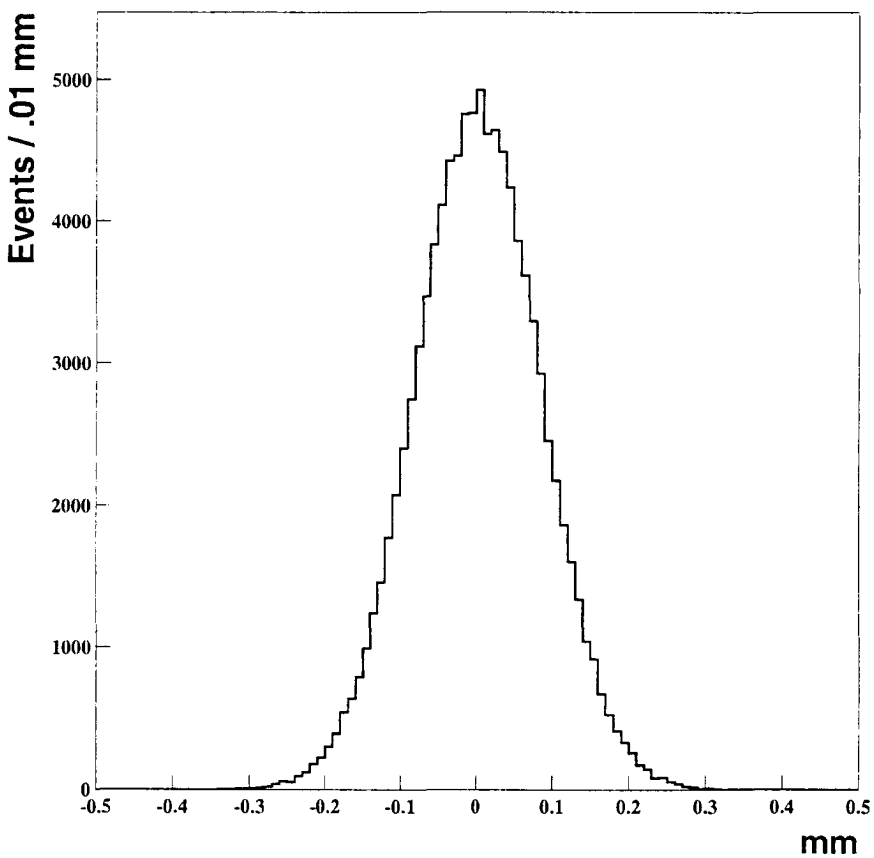

Figure 4.6 MC distribution of the x Position of Ξ^- at the Target for $\Xi^- \to p\mu^-\mu^-$ Events

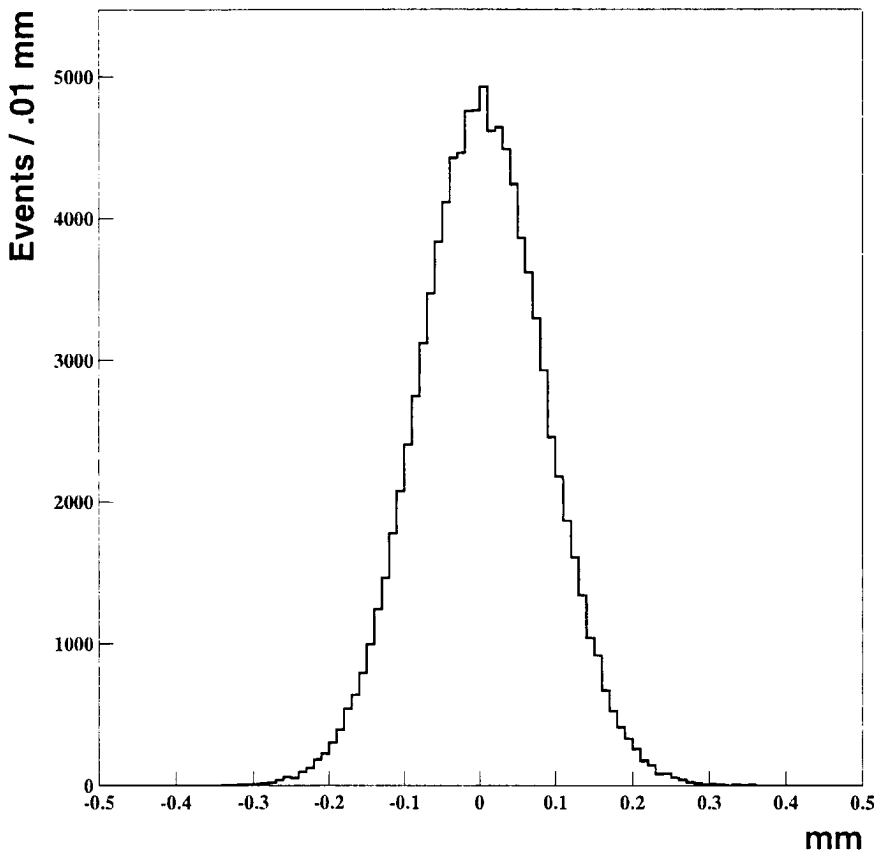

Figure 4.6 MC distribution of the x Position of Ξ^- at the Target for $\Xi^- \to p\mu^-\mu^-$ Events

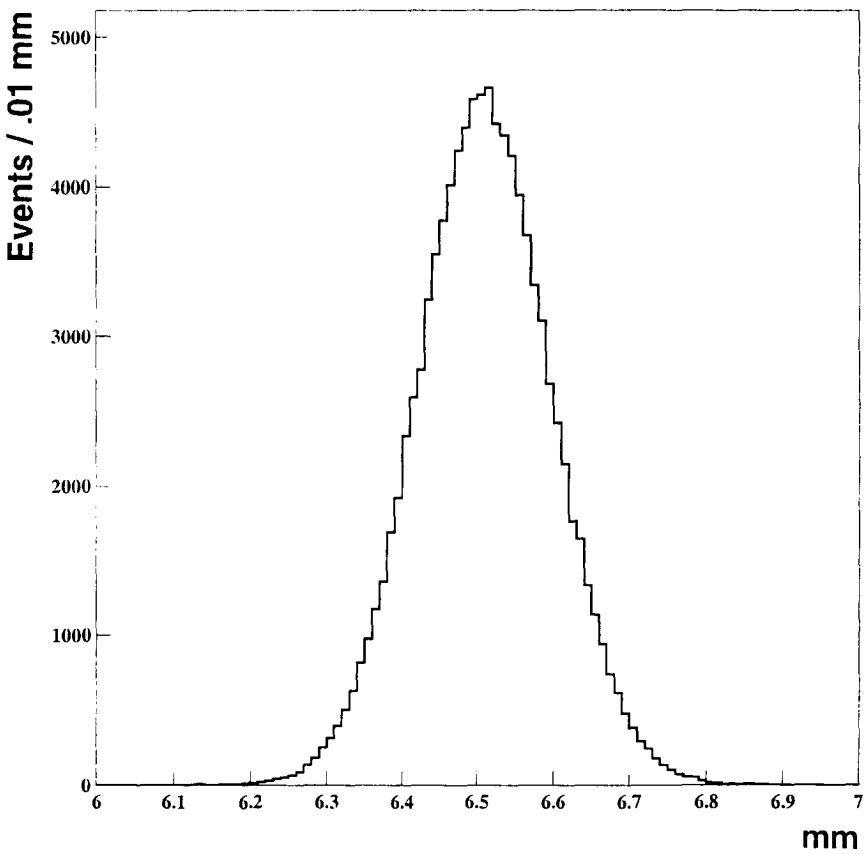

Figure 4.7 MC distribution of the y Position of Ξ^- at the Target for $\Xi^- \to p\mu^-\mu^-$ Events

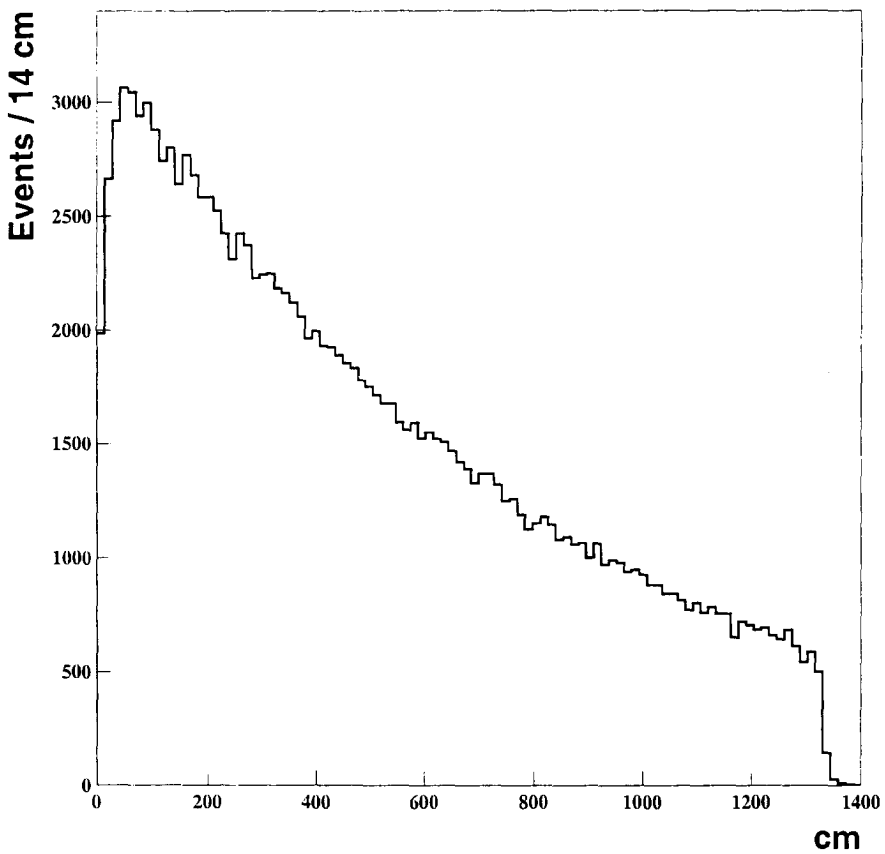

Figure 4.8 MC distribution of the z of the Ξ^- Decay Vertex for $\Xi^- \to p\mu^-\mu^-$ Events

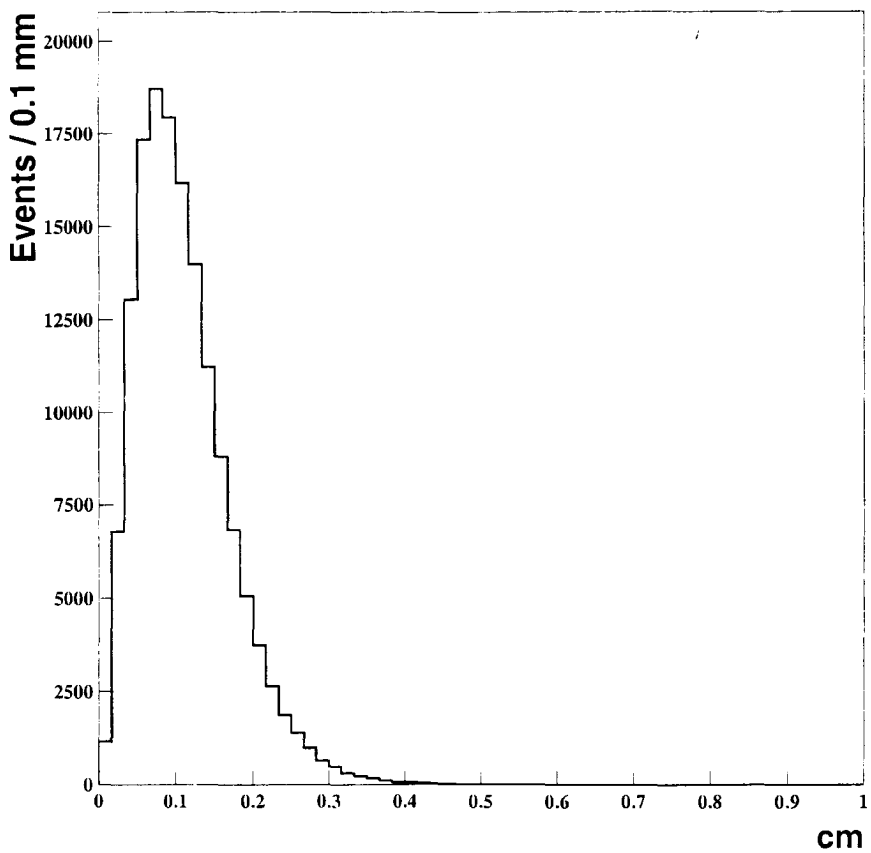

Figure 4.9 MC distribution of the Average Distance between Tracks at the Common Vertex for $\Xi^- \to p\mu^-\mu^-$ Events

Table 4.1 Efficiencies of Cuts for Signal and Normalization Modes.

Parameter	Cut	$p\mu^-\mu^-$ (%)	$\Lambda\pi^-$ (%)
momentum	$120.0 < p_{tot} < 250.0$ GeV/c	99.7	99.5
mom. frac	$\mid p_{os} \mid > 0.6 \mid p_{tot} \mid$	64.9	
x,y tgt	$\mid x_{tgt} \mid < 0.5$ cm $\mid y_{tgt} - 6.55 \mid < 0.5$ cm	99.9	85.4
z decay	$50.0 < z_{vtx} < 1250.0$ cm	90.1	97.4
vtx	$dist < 0.2$ cm $\chi^2 < 2.5$	78.0 99.9	
Λ	$1.1 < m_\Lambda < 1.125$ GeV/c^2	62.4	
K	$0.484 < m_K < 0.502$ GeV/c^2	98.7	
ghosts	$\mid \delta$(dnstrm xslope)$\mid > 0.0001$ $\mid \delta$(dnstrm xint)$\mid > 0.1$ cm	98.0	
		27	81

4.2 Comparison Of MC With Data

It is essential to compare simulated MC events with data collected from the experiment to ensure that the MC does indeed simulate the spectrometer, and the production and decay of the particles in a manner consistent with the data. Since the relative detector acceptances were to be extracted from the MC simulations, it was important that the simulated events match with the data. Since there is no experimental data available for the decay $\Xi^- \to p\mu^-\mu^-$ (because it's an unobserved, forbidden mode) the comparison between MC and data was done for the decay $\Xi^- \to \Lambda\pi^-$, $\Lambda \to p\pi^-$. The Ξ^- hyperons were produced at the target with a production model described in Section 4.1. The production parameters were tuned to match the MC and data samples for Run #2200. Figures 4.10– 4.17 show the comparison between MC and data samples. As can be seen, the distributions match very well. Variations such as those in beam targeting can lead to a mismatch and systematic uncertainties due to the MC were investigated and are discussed in Section 4.6.

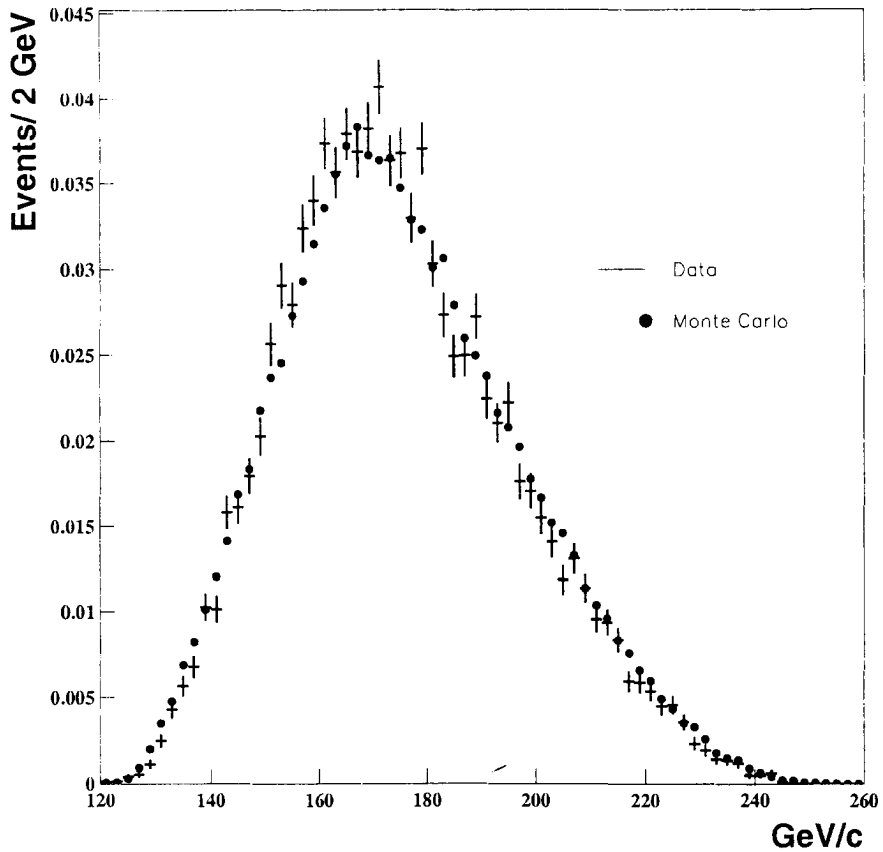

Figure 4.10 MC and Data Distributions of p_{total} for $\Xi^- \to \Lambda\pi^-$ Events after matching for Run #2200

4.3 Normalization

As mentioned earlier, the rate of the decay $\Xi^- \to p\mu^-\mu^-$ will be measured relative to the rate of the normalization mode $\Xi^- \to \Lambda\pi^-$, $\Lambda \to p\pi^-$. This normalization factor can be calculated by knowing

I. number of $\Xi^- \to \Lambda\pi^-$, $\Lambda \to p\pi^-$ decays reconstructed in the spectrometer.

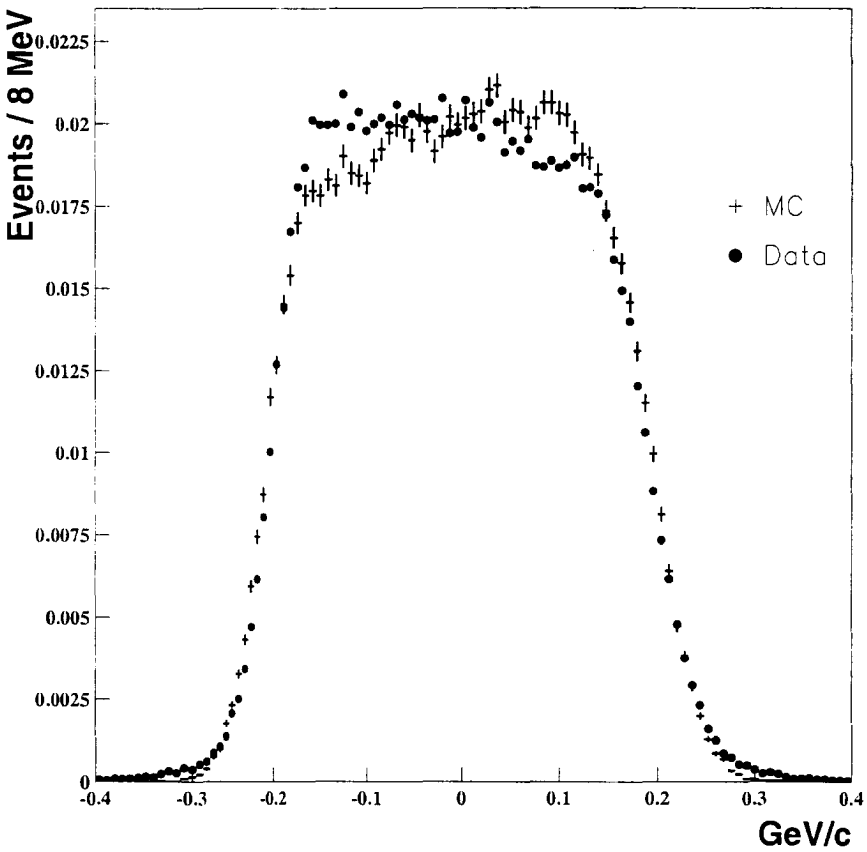

Figure 4.11 MC and Data distributions of p_x for $\Xi^- \to \Lambda\pi^-$ Events

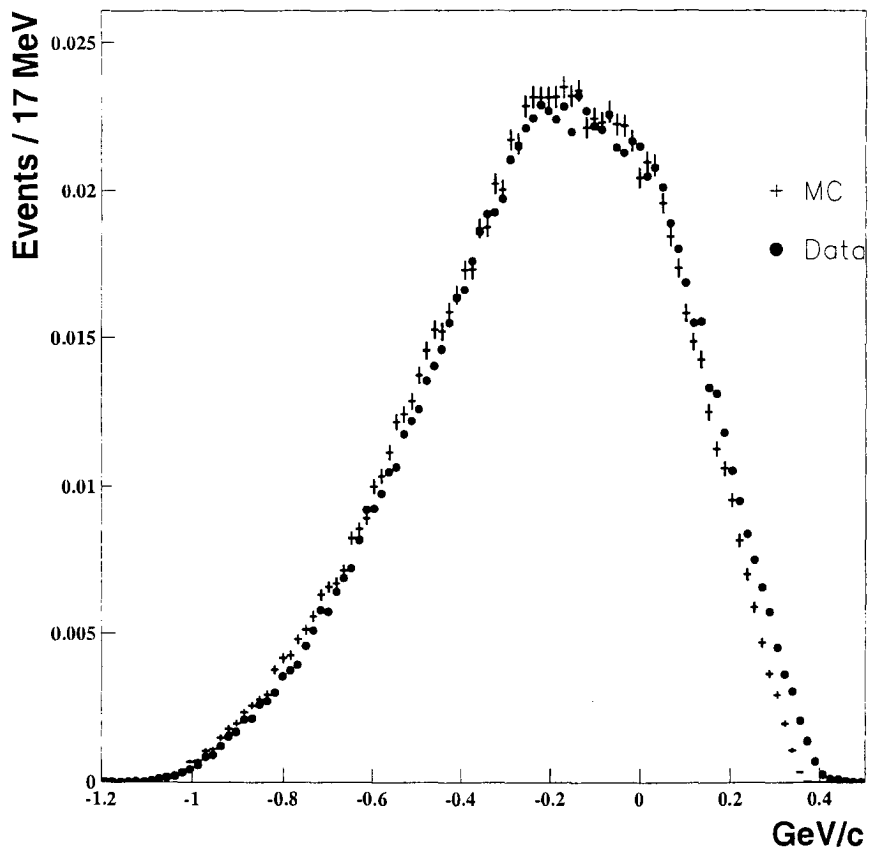

Figure 4.12 MC and data Distributions of p_y for $\Xi^- \to \Lambda\pi^-$ Events

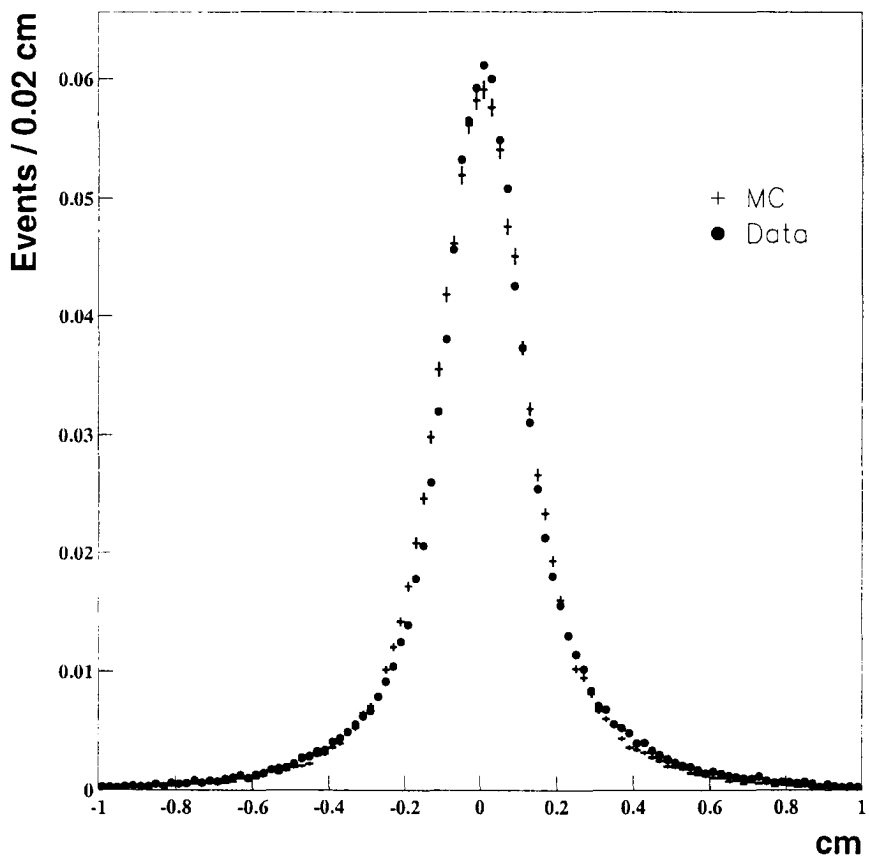

Figure 4.13 MC and Data Distributions of the x Position of the Ξ^- Hyperon at Target, for $\Xi^- \to \Lambda\pi^-$ Events

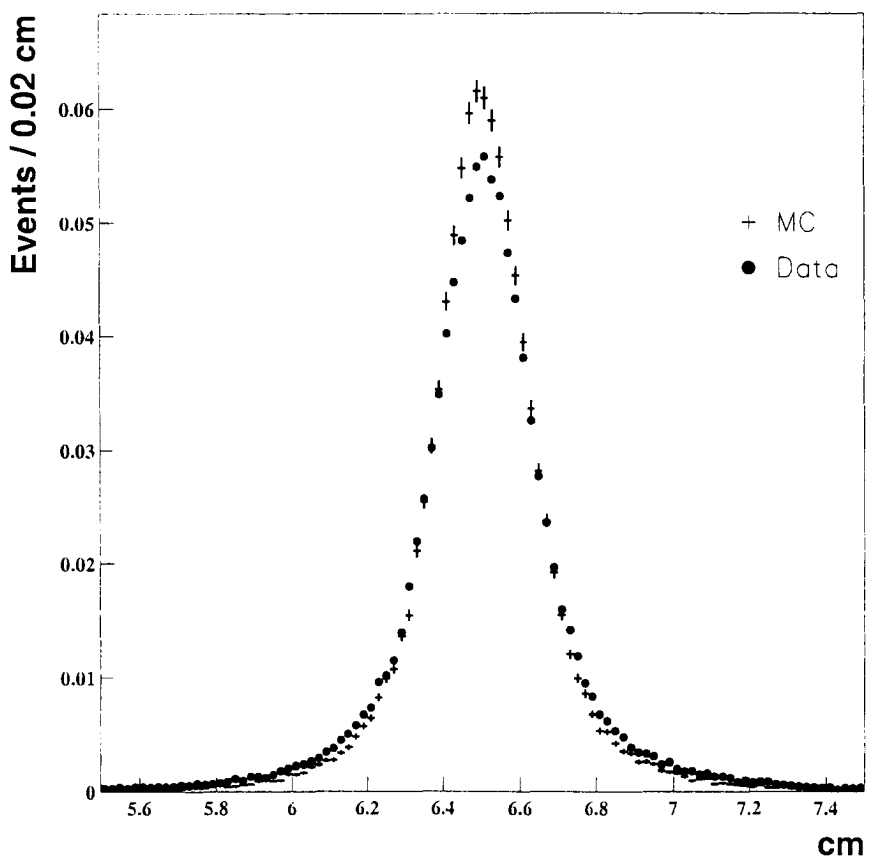

Figure 4.14 MC and Data Distributions of the y Position of the Ξ^- Hyperon at Target, for $\Xi^- \to \Lambda\pi^-$ Events

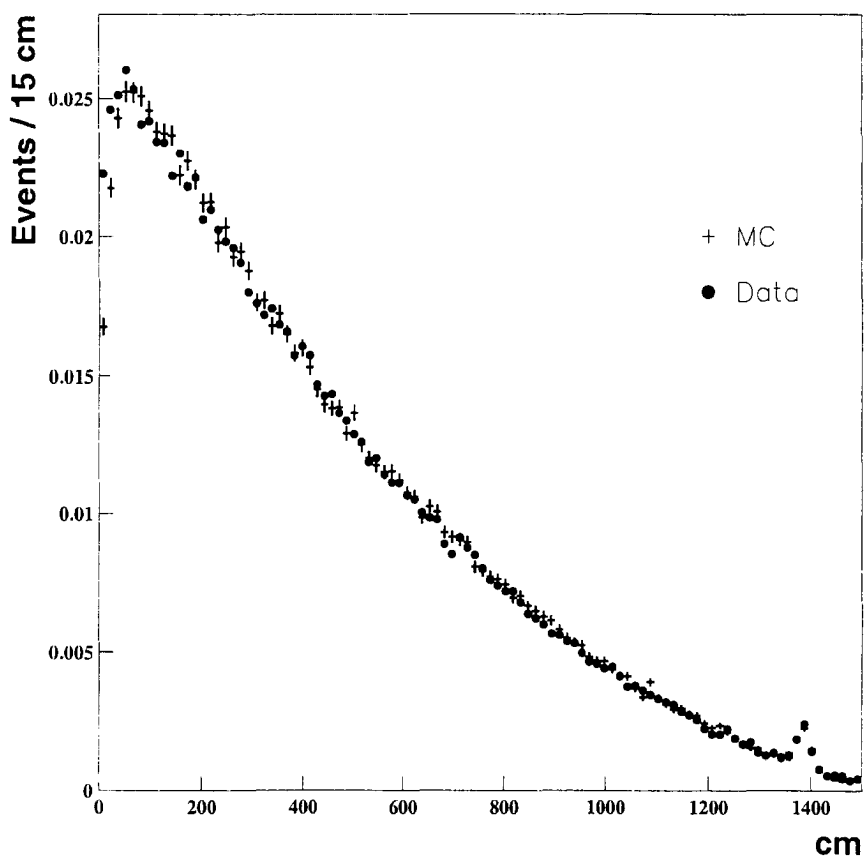

Figure 4.15 MC and Data Distributions of the z Position of the Ξ^- Decay Vertex, for $\Xi^- \to \Lambda\pi^-$ Events

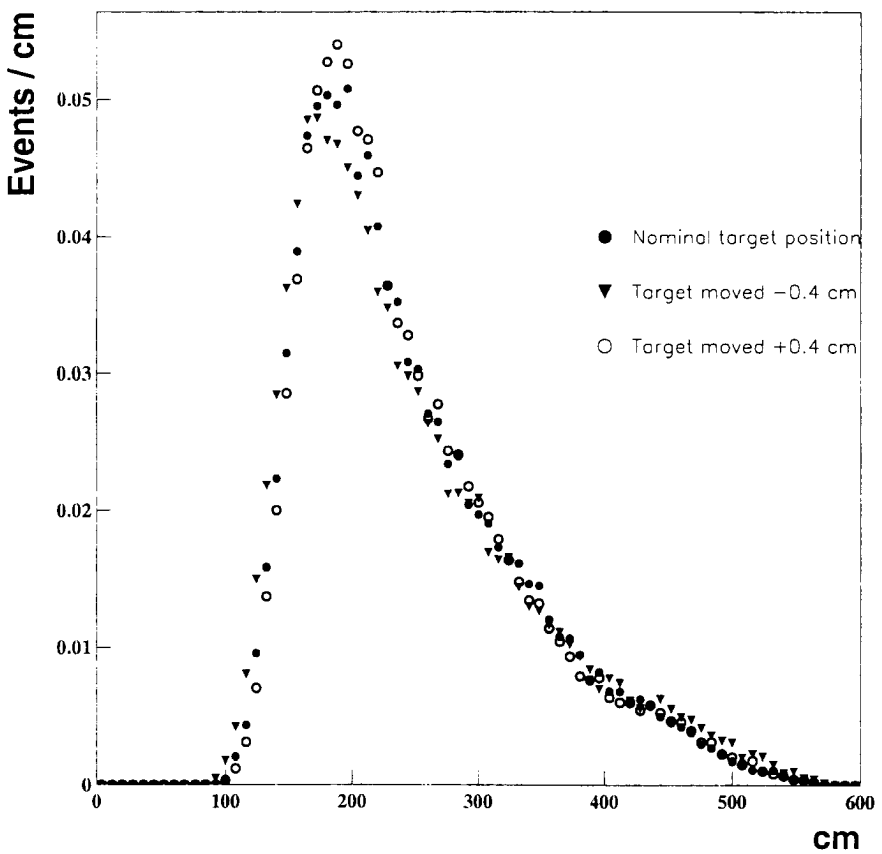

Figure 4.16 MC and Data Distributions of the First Pion at the Location of the Second Muon Steel Block

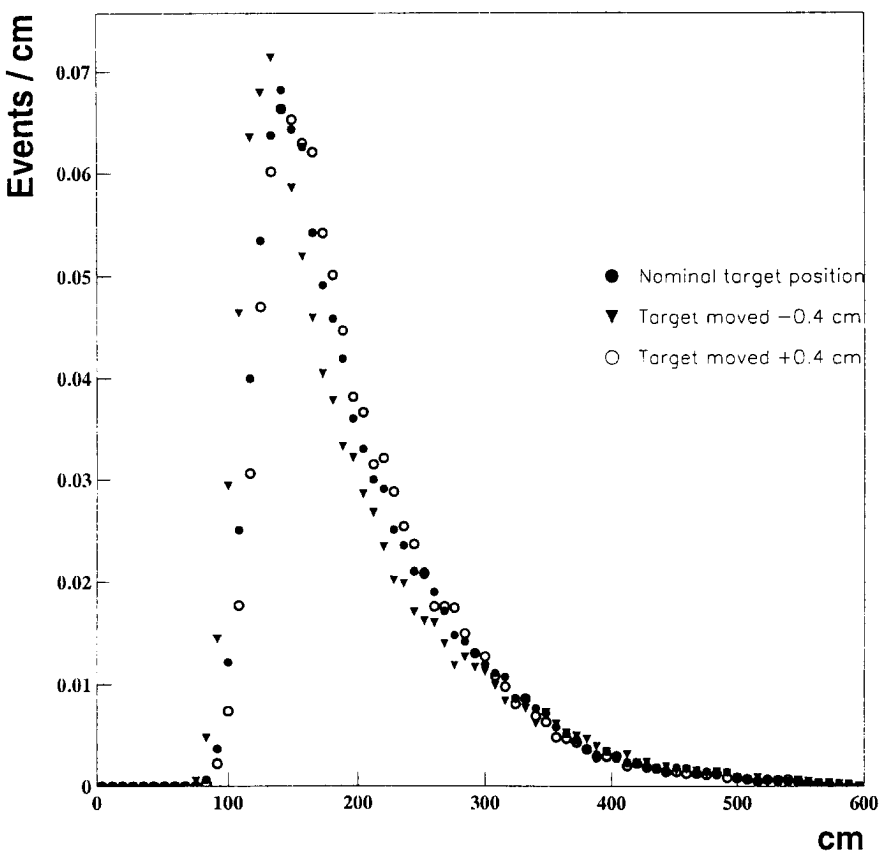

Figure 4.17 MC and Data Distributions of the Second Pion at the Location of the Second Muon Steel Block

II. the reconstruction efficiency for the decays.

III. the branching ratio for the decay.

IV. the fraction of these decays accepted by the geometry of the spectrometer.

The last of these, the geometric acceptance, was calculated by a Monte Carlo simulation of the decay as described earlier, and was found to be 27.4%.

To calculate the total number of reconstructed $\Xi^- \to \Lambda\pi^-$ decays in the experiment, all stream-5 data had to be analyzed. This was because data in stream-7 – the data-set used for the analysis, was pre-selected to have at least one muon track. As a result, not all $\Xi^- \to \Lambda\pi^-$ events would be found in this sample. Stream-5 data, as described earlier in Chapter 3, contained all events with ≥ 3 tracks. All stream-5 data (64 5GB tapes) were processed with a prescale factor of 100 and events satisfying the $\Xi^- \to \Lambda\pi^-$, $\Lambda \to p\pi^-$decay hypothesis were selected. Further, a few selection cuts were made to eliminate background. The efficiencies of the cuts were determined from a MC simulation of the decay (Section 4.2) and are listed in Table 4.1. The only cuts imposed on the normalization sample are those listed in the third column of the table. Figure 4.18 shows the $p\pi^-\pi^-$ invariant mass distribution for the normalization sample. The ratio of signal to background is approximately 2×10^2.

Since the data used for the normalizing and signal modes were on different streams, it was necessary to ensure that the book-keeping was done correctly and that only data corresponding to the signal mode were used for normalization. This was done by making a correspondence between the raw data that produced stream-7 and the corresponding raw inputs to stream-5. A database of the raw inputs for each stream was generated and only events in common to both streams were chosen for the analysis of the signal and normalizing modes. In the final count, after subtracting background, the total number of reconstructed $\Xi^- \to \Lambda\pi^-$, $\Lambda \to p\pi^-$decays was found to be 4.79×10^8. This corresponds to a total of $\sim 14 \times 10^9$ raw input events.

4.4 Backgrounds

As mentioned above the main backgrounds to the $\Xi^- \to p\mu^-\mu^-$ decay is expected to be from the punch-through and decays-in-flight of π^-s from $\Xi^- \to \Lambda\pi^-$ and $K^- \to \pi^-\pi^-\pi^+$ decays. It is important that these backgrounds be understood and properly estimated in order to estimate the rate of the $\Xi^- \to p\mu^-\mu^-$ decay. For the current analysis, the background estimations were done using a MC. 1 million $\Xi^- \to \Lambda\pi^-$ and $K^- \to \pi^-\pi^-\pi^+$ events were generated with the two pions on the SS side (π^-) allowed to decay in flight to $\mu^-\overline{\nu}$. These events were then passed through the set of selection cuts described in Chapter 3 and the surviving events were reconstructed under a $p\mu^-\mu^-$ hypothesis. No events were found in the search region of the resulting invariant mass distribution.

4.5 Triggers

No trigger requirement was imposed on either the signal or the normalizing mode. Since stream-5 data did not contain information about the triggers it was not possible to impose such a requirement on the normalizing mode. However, from Monte Carlo simulations of the decays, it was seen that > 99 % of $\Xi^- \to p\mu^-\mu^-$ decays met the geometric and energy requirements necessary to satisfy the CAS and K triggers. Since most of the $\Xi^- \to \Lambda\pi^-$, $\Lambda \to p\pi^-$decays come under the CAS and K triggers, the acceptances for both modes are similar and the relative trigger inefficiencies would cancel out. The Monte Carlo was also used to check the spatial distribution of protons from the $\Xi^- \to p\mu^-\mu^-$ decay at the calorimeter location to see if it was similar to the corresponding distribution for the normalizing decay. This is important to ensure that the variations in production and efficiencies would affect both modes similarly. As can be seen from Figures 4.19 and 4.20, the protons from both decays are distributed well within the calorimeter volume. The differences between the two distributions are due to the slightly different production and decay kinematics. The systematic uncertainty due to these effects is described in Section 4.6.

4.6 Systematics

In the course of the experiment there were variations in running conditions – *e.g.*, targeting the proton beam, variations in magnetic field, varying detector efficiencies – and these may have an effect on the analysis. In principle, if the variations are known exactly, they can be corrected for. However, it is easier to study the effect of such variations with a MC simulation and quantify the effect as a systematic uncertainty in the measurement. For the present analysis, the primary concern is the relative acceptance between the $\Xi^- \to p\mu^-\mu^-$ and $\Xi^- \to \Lambda\pi^-$ modes. The effect of targeting variations on the relative acceptance is shown in Figures 4.21 and 4.22. The position of the target was varied by $\pm$ 0.5 cm, in steps of 1 mm, in both x and y directions and the geometric detector acceptance was calculated at each position. This was done for both $\Xi^- \to p\mu^-\mu^-$ and $\Xi^- \to \Lambda\pi^-$ modes and the relative acceptance was extracted. As Figure 4.21 shows, the effect of targeting variations is negligible for variations in x, while for the y position, there appears to be an effect creeping in at higher y values. However, the relative acceptance is stable to within $\sim$ 3%.

Since the search for the signal mode relies on information recorded by the muon detection system, variations in muon proportional tube and hodoscope efficiencies would have an effect on the efficiency for selecting muons. To understand and account this source of systematic uncertainty, we performed a study on variations in muon detector efficiencies. Figures 4.23– 4.25 show the variation in individual muon detector efficiencies for the x and y views. The efficiencies are plotted as a function of run number and enable one to see the variation over the course of the entire '97 run of HyperCP. The method employed to determine the efficiency for the muon detector elements has already been described in Chapter 3. The average efficiency for each view was extracted from the distribution and the efficiencies were then used to calculate the overall efficiency for identifying muons. Deviations from the average were designated as systematic uncertainties in the measurement. The overall systematic uncertainty due to variations in muon detector efficiencies was estimated to be $\sim$ 1%

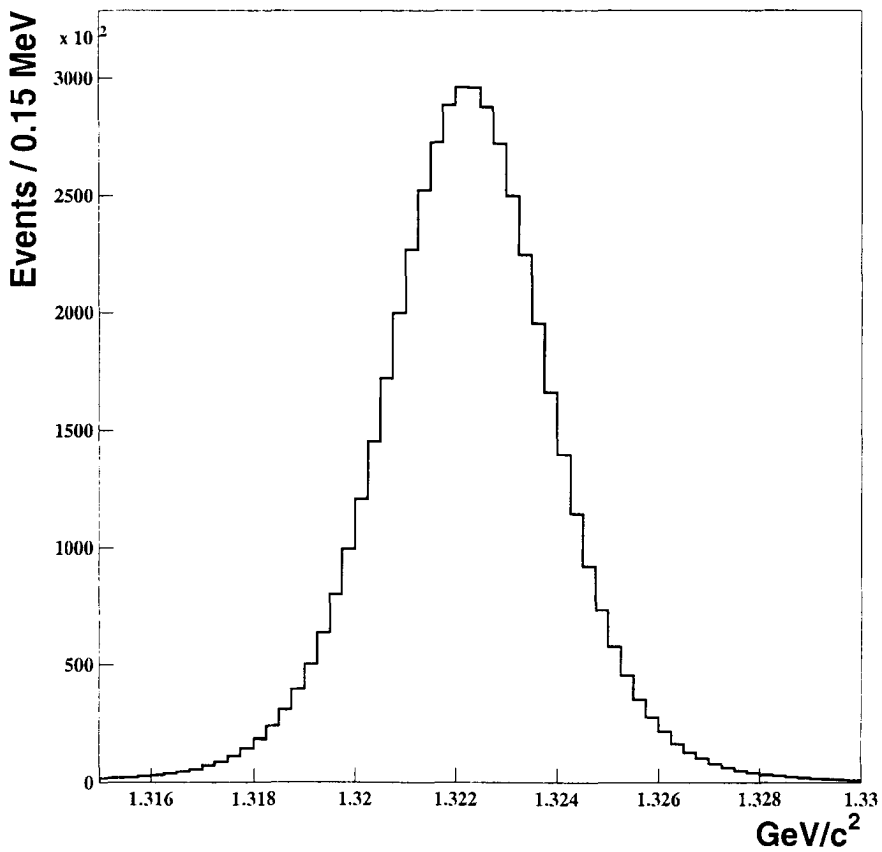

Figure 4.18 Invariant $p\pi^-\pi^-$ Mass Distribution. This is the Normalization Data-set

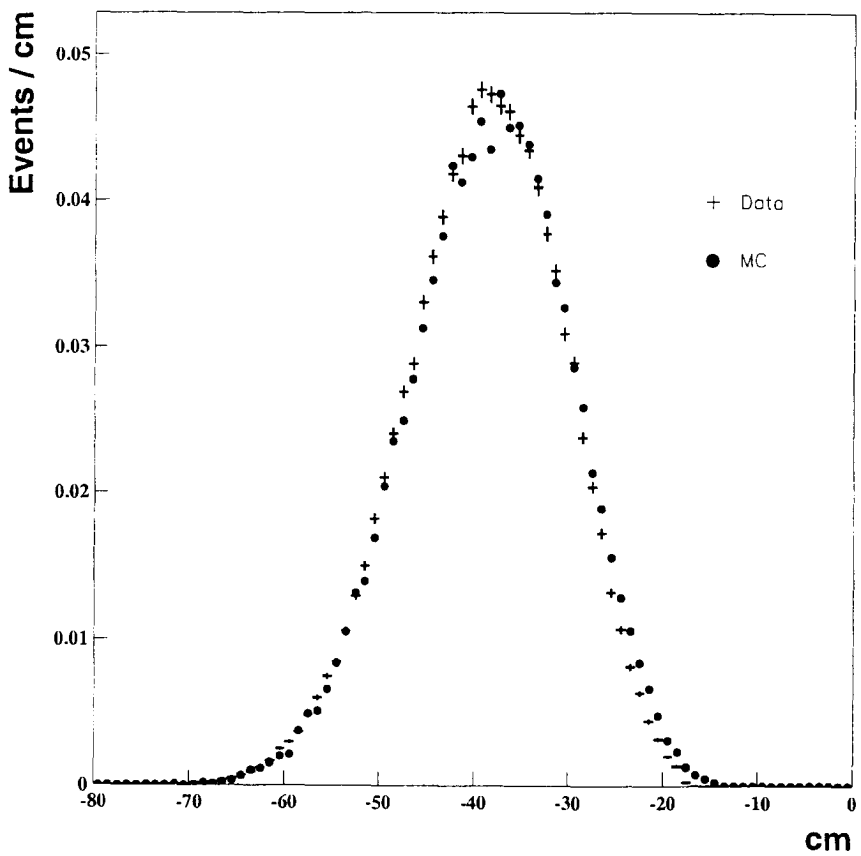

Figure 4.19 x Distribution of the the Proton from $\Xi^- \to \Lambda\pi^-$, $\Lambda \to p\pi^-$ at the Front Face of the Calorimeter

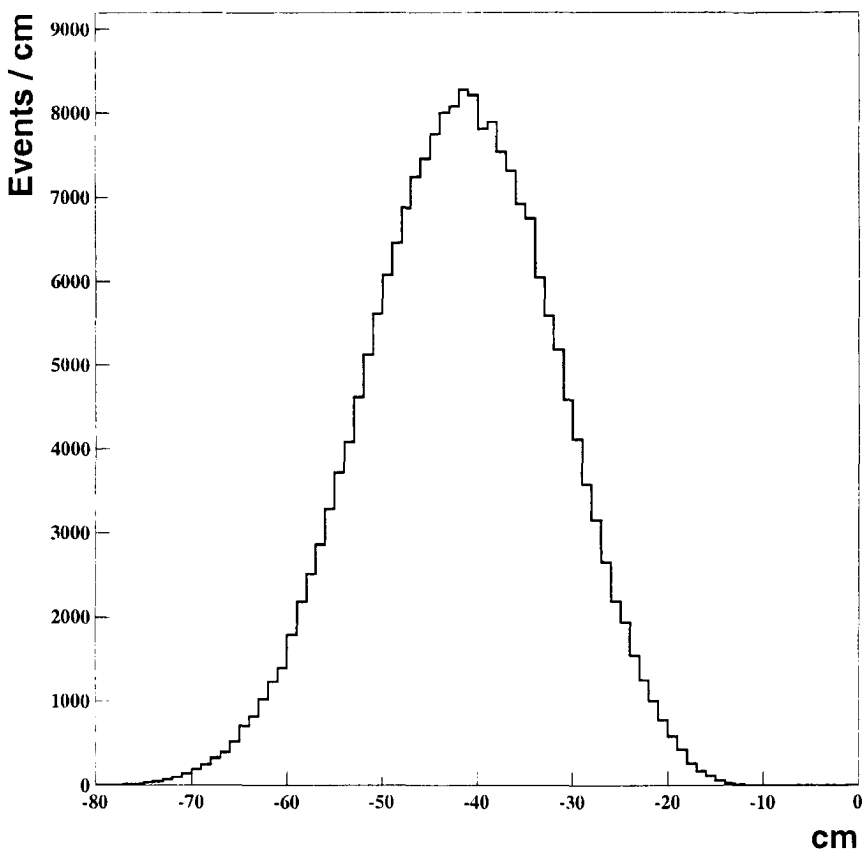

Figure 4.20 x Distribution of the Proton from $\Xi^- \to p\mu^-\mu^-$ at the Front Face of the Calorimeter

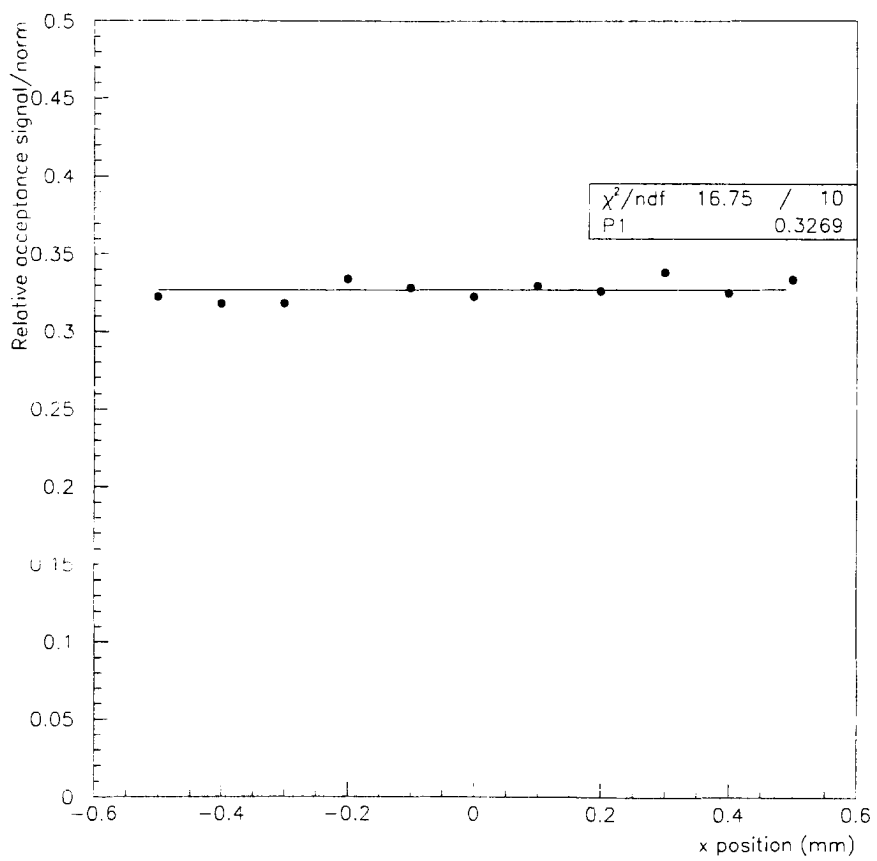

Figure 4.21 Variation in Relative Acceptance between $\Xi^- \to p\mu^-\mu^-$ and $\Xi^- \to \Lambda\pi^-$ Modes Due to Variation in Beam Targeting in x

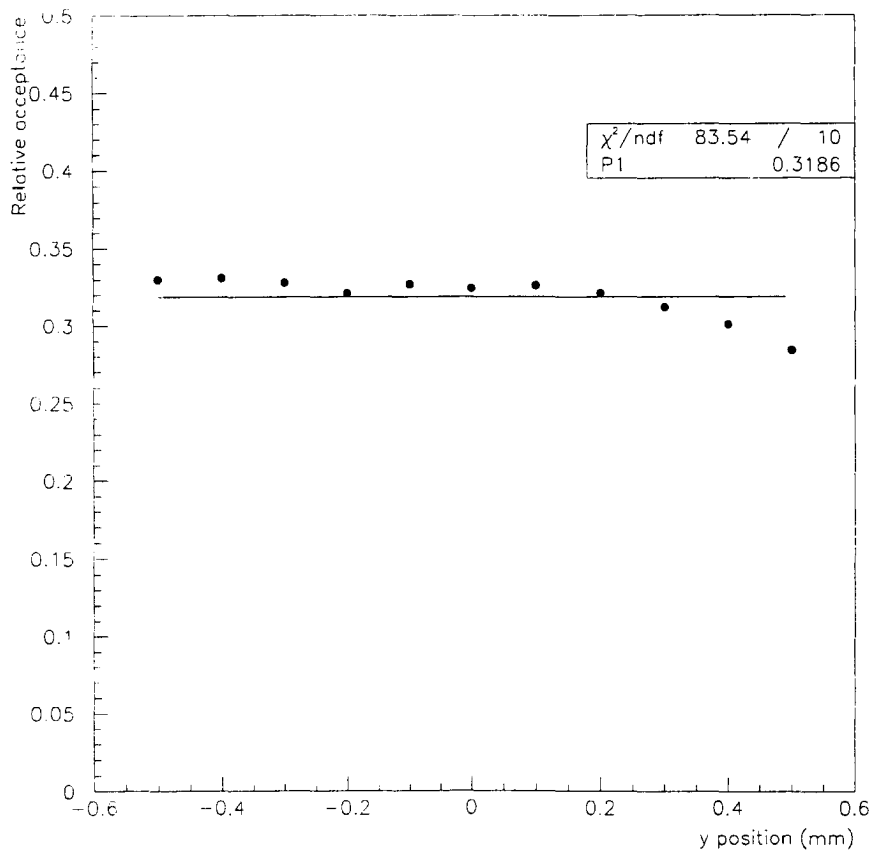

Figure 4.22 Variation in Relative Acceptance between $\Xi^- \to p\mu^-\mu^-$ and $\Xi^- \to \Lambda\pi^-$ Modes Due to Variation in Beam Targeting in y

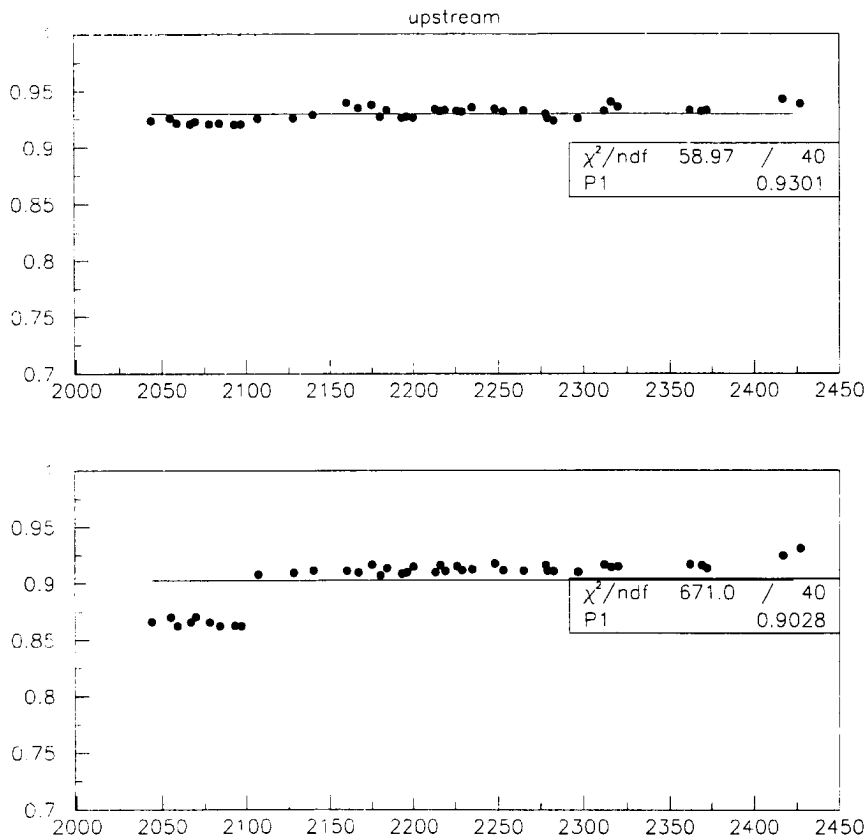

Figure 4.23 Distribution of Upstream Muon Proportional Tube Efficiencies as a Function of Run Number. The Top Plot Shows the Distribution for the x View and the Bottom Plot Shows the Distribution for the y View

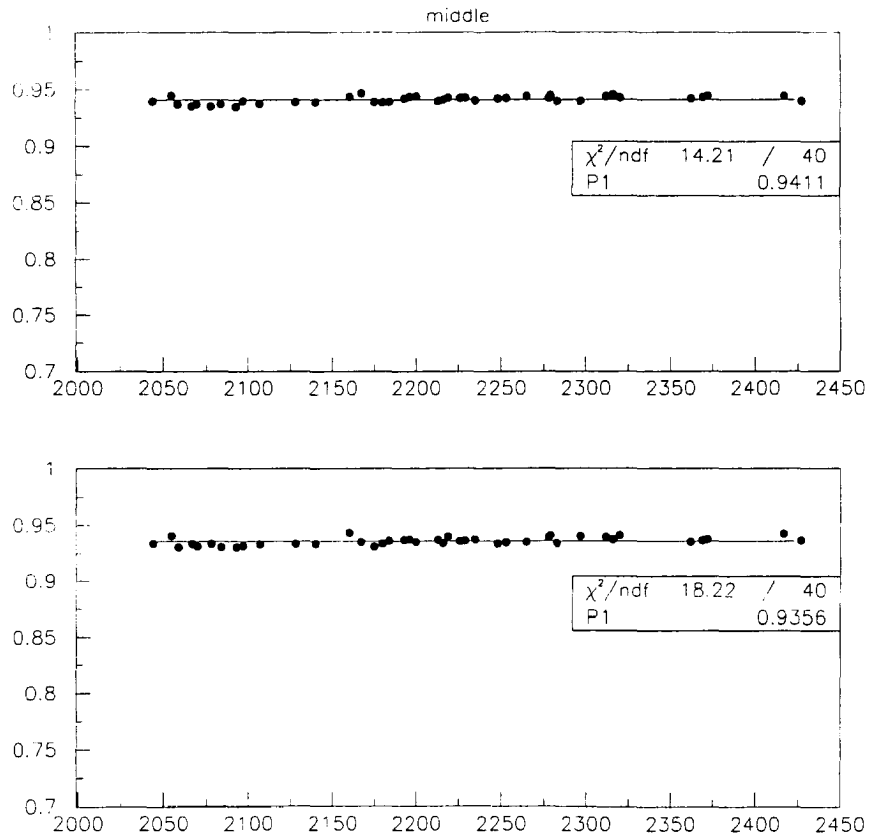

Figure 4.24 Distribution of Midstream Muon Proportional Tube Efficiencies as a Function of Run Number. The Top Plot Shows the Distribution for the x View and the Bottom Plot Shows the Distribution for the y View

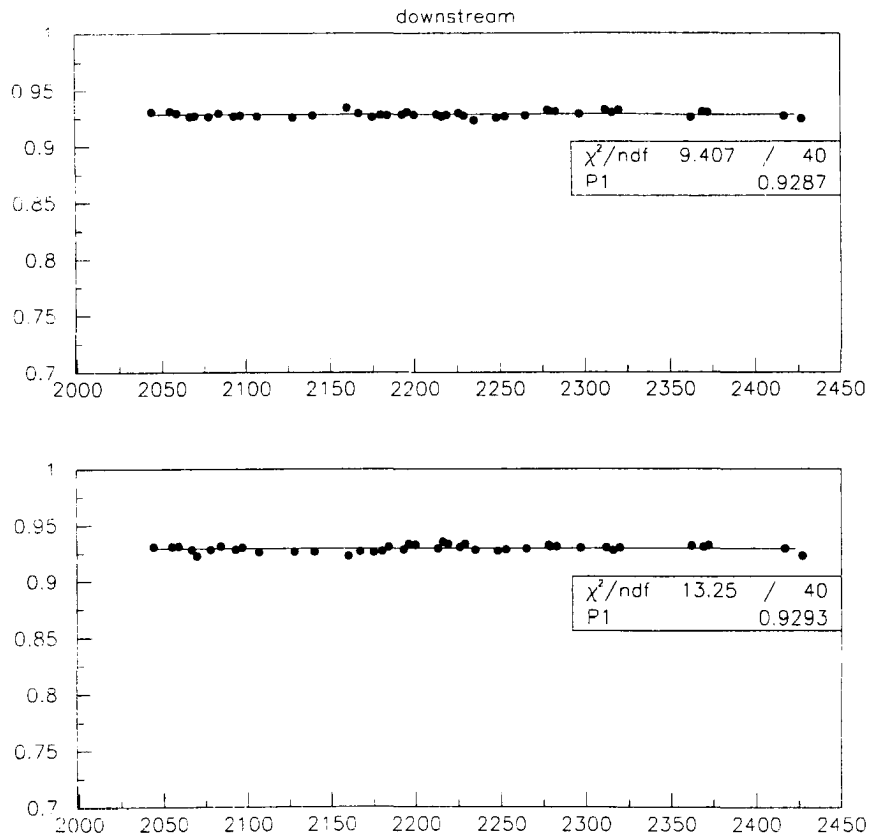

Figure 4.25 Distribution of Downstream Muon Proportional Tube Efficiencies as a Function of Run Number. The Top Plot Shows the Distribution for the x View and the Bottom Plot Shows the Distribution for the y View

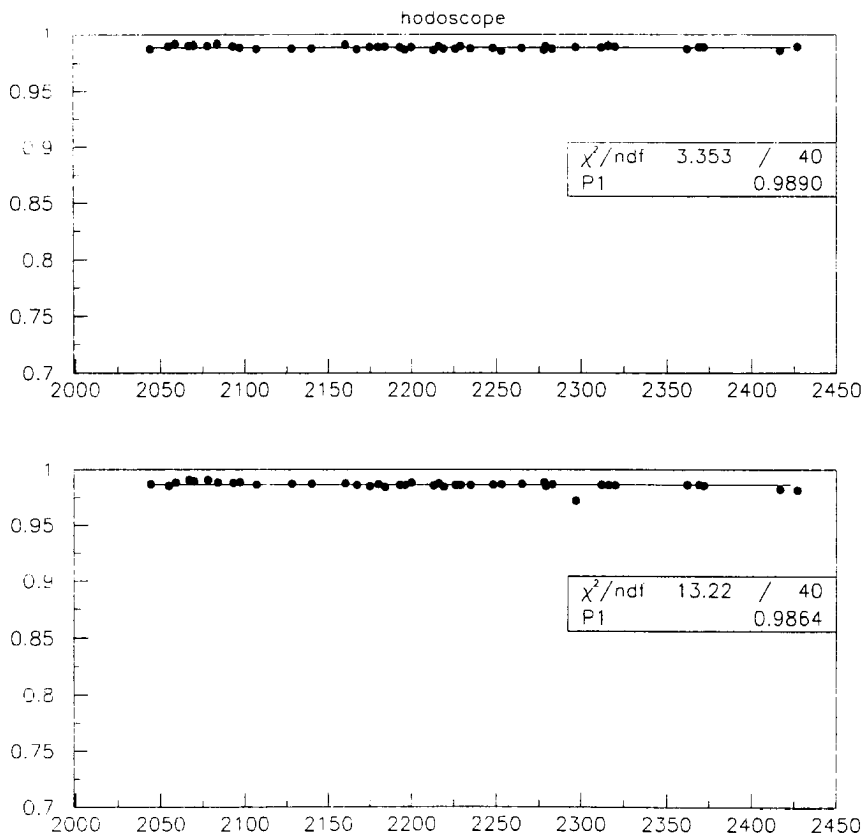

Figure 4.26 Distribution of Muon Hodoscope Efficiencies as a Function of Run Number. The Top Plot Shows the Distribution for the x View and the Bottom Plot Shows the Distribution for the y View

MC simulations are themselves another source of systematic uncertainty which was studied. The tunable parameters in the MC model for producing Ξ^- hyperons at the target were varied and as with other systematic studies the effect of the variations on the relative acceptance between signal and normalizing modes were studied. In the simple model used for generating Ξ^- hyperons at the target, the exponent n in the distribution of the invariant production cross-section was chosen to be 1. In our systematic studies we varied this parameter in the range $0.5 < n < 1.5$. In this range the variation in the relative acceptance was found to be 3%.

One final systematic effect to be taken into account is the uncertainty in the normalization factor. The primary uncertainty in estimating the number of normalizing decays is in the background to the $\Xi^- \to \Lambda\pi^-$ decay and from the fit this was estimated to be 1.5%. The systematic effects are summarized in Table 4.3. From the individual systematic uncertainties in our analysis (listed in Table 4.3) the overall systematic uncertainty was calculated to be 4.3%.

4.7 Calculating The Branching Ratio

Figure 4.27 shows the final $p\mu^-\mu^-$ invariant mass distribution after the application of all selection cuts. As can be seen, there is 1 event within $\pm 3\sigma$ of the Ξ^- mass. By looking at the distribution of events in the region $1.28 < m_{p\mu^-\mu^-} < 1.4$ GeV/c^2, this one event is consistent with background. Since the number of observed events is small and governed by Poisson statistics, we can calculate an upper limit on the branching ratio

$$\frac{B(\Xi^- \to p\mu^-\mu^-)}{B(\Xi^- \to \Lambda\pi^-)}$$

as described below.

$$\frac{B(\Xi^- \to p\mu^-\mu^-)}{B(\Xi^- \to \Lambda\pi^-)} = \frac{n_{\Xi^- \to p\mu^-\mu^-}}{n_{\Xi^- \to \Lambda\pi^-}} \times (\epsilon_{relative}) \times \frac{1}{B(\Lambda \to p\pi^-)}$$

Table 4.2 Relative efficiencies for the detection of $\Xi^- \rightarrow \Lambda\pi^-$ and $\Xi^- \rightarrow p\mu^-\mu^-$ decay modes

Factor	Efficiency for $\Xi^- \rightarrow p\mu^-\mu^-$	Efficiency for $\Xi^- \rightarrow \Lambda\pi^-$
Geometric acceptance	9.3%	27.4%
Reconstruction	87.8%	87.4%
Selection cuts	27.3%	81.1%
Muon Selection	84.5%	

where

$$n_{\Xi^- \rightarrow p\mu^-\mu^-} = \text{Number of observed } \Xi^- \rightarrow p\mu^-\mu^- \text{ events}$$

$$n_{\Xi^- \rightarrow \Lambda\pi^-} = \text{Number of events in the normalization mode}$$

$$\epsilon_{relative} = \frac{\epsilon_{\Xi^- \rightarrow \Lambda\pi^-}}{\epsilon_{\Xi^- \rightarrow p\mu^-\mu^-}}$$

The efficiency (ϵ) for the detection of either mode is the combination of the geometric acceptance for the decay mode, the efficiency of reconstructing the decay, the overall efficiency of the selection cuts, and the efficiency for particle identification. These individual factors have already been discussed earlier and are summarized in Table 4.2.

From the table of confidence intervals for Poisson statistics for small samples [25], it can be seen one observed event with an expected background of one event translates to 3.2 observed events ($n_{\Xi^- \rightarrow p\mu^-\mu^-}$) at a 90% confidence limit. As mentioned earlier, the number of decays in the normalization mode was calculated to be 4.79×10^8, and the relative acceptance between the two modes was found to be 2.94. Finally, the branching fraction for $\Lambda \rightarrow p\pi^-$ is 0.64 [26].

Based on these calculations, an upper limit on the branching ratio was calculated to be

Table 4.3 Summary of Systematic Uncertainties

Factor	Systematic effect
Beam targeting	2.1%
Normalization	1.7%
MC Simulation	3.1%
Muon selection	1.4%

$$\frac{B(\Xi^- \to p\mu^-\mu^-)}{B(\Xi^- \to \Lambda\pi^-)} < \frac{n_{\Xi^- \to p\mu^-\mu^-}}{n_{\Xi^- \to \Lambda\pi^-}} \times (\epsilon_{relative}) \times \frac{1}{B(\Lambda \to p\pi^-)}$$

$$< \frac{3.2}{4.79 \times 10^8} \times 2.94 \times \frac{1}{0.64}$$

$$< 1.06 \times 10^{-7}$$

at the 90% confidence limit. The systematic uncertainty in the measurement, as mentioned in Section 4.6 was 4.3 %.

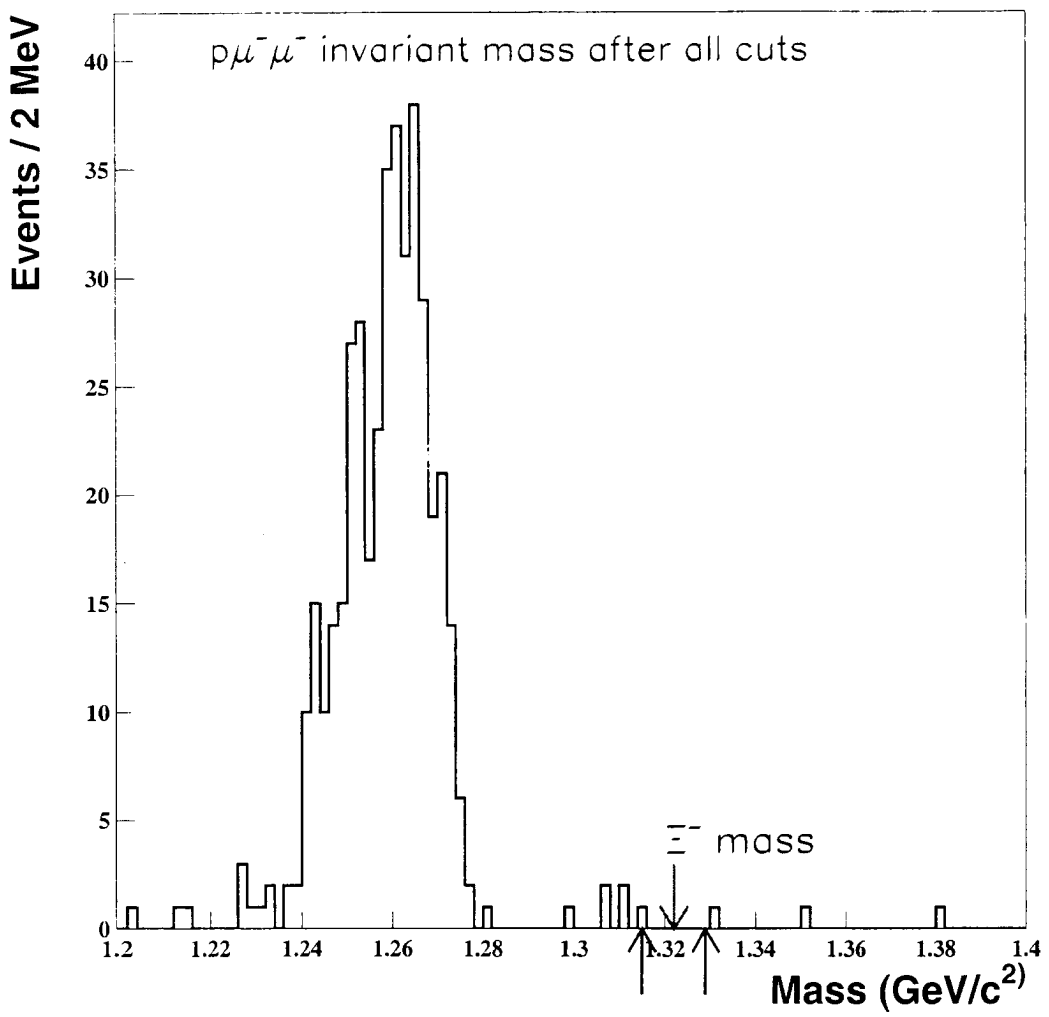

Figure 4.27 $p\mu^-\mu^-$ Invariant Mass Distribution After Applying All Selection Cuts

CHAPTER V

CONCLUSION

From our analysis of Run I data from HyperCP, we see no signal for the lepton-number-violating $\Xi^- \to p\mu^-\mu^-$ decay. Based on 4.79×10^8 normalizing $\Xi^- \to \Lambda\pi^-$, $\Lambda \to p\pi^-$ decays, we have set an upper limit on the branching ratio:

$$\frac{B(\Xi^- \to p\mu^-\mu^-)}{B(\Xi^- \to \Lambda\pi^-)} < (1.06 \pm 0.04) \times 10^{-7}$$

at 90% confidence. This is more than three orders of magnitute better than the current limit of $< 4 \times 10^{-4}$ and is the most stringent bound on $\Delta L = 2$ processes in the hyperon sector. The systematic error in our measurement was dominated by uncertainties due to the Monte Carlo simulations of the decays and uncertainties due to beam targeting. However, the limiting factor was statistics due to the number of normalizing decays.

Our analysis is based only on the negatively charged Ξ hyperons from Run I of HyperCP. Run II of HyperCP gathered ~ 2.5 times more data than Run I. Adding data from both runs to the analysis sample would thus make the search for the decay more sensitive by as much as a factor of 2.5.

There exists no theoretical model or calculation of the rate for the $\Xi^- \to p\mu^-\mu^-$ decay. Difficulties in calculating the hadronic matrix element involved make evaluating Figure 1.1 complicated. Also, an upper limit on the branching ratio cannot be directly translated to an upper limit on the mass of the neutrino involved. If one had a model for the decay and knew the hadronic matrix element, then analagous to neutrinoless double-beta decays, one could place a constraint on $\sum_i U_{\mu i}^2 m_{\nu_i}$, where $U_{\mu i}$ are the lepton mixing matrix coefficients.

Another approach to studying the $\Delta L = 2$ processes is to utilize the HyperCP data to perform a search for the similar lepton-number-violating decay of the Σ^- hyperon: $\Sigma^- \to p\mu^-\mu^-$. This decay is a $\Delta S = 1$ transition, unlike the $\Delta S = 2$ transition of the $\Xi^- \to p\mu^-\mu^-$ decay, and would be less suppressed. HyperCP should have a large number of Σ^- decays in the spectrometer. While the number of Σ^-'s could potentially be more than the number of Ξ^-'s, an accurate counting of the number of normalizing Σ^- decays ($\Sigma^- \to n\pi^-$) may be difficult since the HyperCP spectrometer was not designed for tracking neutral particles. However it could still be a sensitive search for lepton-number-violation in hyperons and one worth exploring.

REFERENCES

[1] Lincoln Wolfenstein, Lepton Number Violation and Neutrino Mass, *Neutrino:84* (1984), p. 730.

[2] Zee, A., A Theory of Lepton Number Violation, Neutrino Majorana mass, and Oscillation, *Phys. Lett.*, **B93**, 389, (1980).

[3] Edward Witten, Lepton Number and Neutrino Masses, *Nucl. Phys. Proc. Supplement*, **91**, (2000), p. 3.

[4] Glashow, S.L., Partial Symmetries of Weak Interactions, *Nucl. Phys.*, **22**, (1961), pp. 579-588.

[5] Weinberg, S., A Model of Leptons, *Phys. Rev. Lett.*, **19**, (1967), p. 1264.

[6] Salam, A., *Elementary Particle Theory*, (Almquist and Wiksells, Stockholm), (1969), p. 367.

[7] Cabibbo, N., Unitary Symmetry and Leptonic Decays, *Phys. Rev. Lett.*, **10**, (1963), pp. 531-532.

[8] Kobayashi, M. and Maskawa, T., CP Violation in the Renormalizable Theory of Weak Interaction, *Prog. Theor. Phys.*, **49**, (1973), pp. 652-657.

[9] Fukuda, Y., *et. al.*, Evidence for Oscillation of Atmospheric Neutrinos, *Phys. Rev. Lett.*, **81**, (1998), pp. 1562-1567.

[10] Hatakeyama, S., *et. al.*, Kamiokande Collaboration, Measurement of the Flux and Zenith Angle Distribution of Upward Through Going Muons in Kamiokande II + III, *Phys. Rev. Lett*, **81**, (1998), p. 2016.

[11] Athanassopoulos, C., *et. al.*, LSND Collaboration, Evidence for Nu(Mu)to Nu(E) Neutrino Oscillations from LSND, *Phys. Rev. Lett*, **81**, (1998), pp. 1774-1777.

[12] SNO Collaboration, Measurement of the Charged Current Interactions Pro duced by Solar Neutrinos at the Sudbury Neutrino Observatory, *Phys. Rev. Lett.*, **87**, (2001), p.7031.

[13] Weinberg, S., Baryon and Lepton Nonconserving Processes, *Phys. Rev. Lett.*, **43**, (1979), pp. 1566-1570; Barbieri, R., Ellis, J., and Gaillard, M., Neutrino Masses and Oscillations in SU(5), *Phys. Lett.*, **B90**, (1980), pp. 249-256.

[14] Gell-Mann, M., Ramond, P., and Slansky, R., Complex Spinors and Unified Theories, Stony Brook Workshop, (1979); Yanagida, T., *Proc. of the Workshop on Unified Theories and Baryon Number in the Universe*, KEK, Japan (1979); J. L. Chkareuli, J.L., Gogoladze, I.G., Kobakhidze, A.B., Towards the Nonchiral Extension of SM and MSSM, *Phys. Lett.*, **B376**, (1996), pp. 111-118

[15] Gelmini, G.B. and Roncadelli, M., Lefthanded Neutrino Mass Scale and Spontaneously Broken Lepton Number, *Phys. Lett.*, **B99**, (1981), pp. 411-423.

[16] Majorana, E., Theory of the Symmetry of Electrons and Positrons, *Nuovo. Cim.*, **14**, (1937), pp. 171-184.

[17] Schechter, J. and Valle, J.W.F., Neutrinoless Double Beta Decays in SU(2) x U(1) Theories, *Phys. Rev. D*, **25**, (1982), pp. 2951-2963.

[18] Klapdor-Kleingrothaus, H.V., *Proc. Int. Workshop on Particle Physics Beyond the Standard Model*, Castle Ringberg (1997).

[19] Heidelberg-Moscow Collaboration, Limits on the Majorana Neutrino Mass in the 0.1ev Range, *Phys. Rev. Lett.*, **83**, (1999), p. 41.

[20] Cheng, T.P. and Li, L.F., Neutrino Masses, Mixings and Oscillations in SU(2) x U(1) Models of Electroweak Interactions, *Phys. Rev. D*, **22**, (1980), pp. 2860-2887; Babu, K., Model of Calculable Majorana Neutrino Masses, *Phys. Lett.*, **B203**, (1988), pp. 132-144.

[21] Littenberg, L. and Shrock, R., Upper Bounds on Delta L = 2 Decays of Baryons, *Phys. Rev. D*, **46**, (1992), pp. 892-894.

[22] Yeh, N., Gaigalas, A., Smith, W.D., Zendle, H., Baltay, C., Bridgewater, A., Csorna, S., Cooper, W.A., Gershwin, L.K., Habibi, M., Kalelkar, M., Observation of Rare Decay Modes of the XI Hyperons, *Phys. Rev. D*, **10**, (1974), pp. 3545-3584.

[23] Chen, Y.C., Choong, W.S., Dukes, E.C., Gu, P., Ho, C., James, C., Kaplan, D.M., Luebke, W.R., Luk, K.B., Nelson, K., Rubin, H.A., Sheng, J.P., White, C.W., Yu, C.S., A High-Throughput Data Acquisition System for the HyperCP Experiment, *Nucl. Instrum. Meth.*, **A455**, (2000), p. 424-432.

[24] Breitung, M., Fromm, J., Levshina, T., Mandrichenko, I., Schweitzer, M., Farm Batch System and Fermi Inter-Process Communication and Synchronization, CHEP (2000).

[25] Feldman, G.J. and Cousins, R.D., A Unified Approach to the Classical Statistical Analysis of Small Signals, *Phys. Rev. D*, **57**, (1998), pp. 3873-3889.

[26] Particle Data Group., Review of Particle Physics, (2000).